

**CFD modeling of geobag stability for riverbank erosion protection  
structures**

by

Saman Shabani

A thesis submitted in partial fulfillment of the requirements for the degree of

Master of Science

Department of Mechanical engineering  
University of Alberta

© Saman Shabani, 2023

# Abstract

Riverbank erosion poses significant environmental and infrastructural challenges, including soil loss, damage to infrastructure, flooding, and threats to wildlife and vegetation. Erosion control structures are essential for mitigating this issue, and geobags have been used as a fundamental element of revetment structures since the 1970s. The use of geobags offers numerous advantages over traditional rip-rap, such as long-term durability, cost-efficiency, eco-friendliness, and environmental safety. One of the key benefits of geobag revetments is the stability they provide for communities living along riverbanks, fostering economic development in the surrounding areas. To ensure the effective design of such structures, a comprehensive understanding of geobag stability under hydraulic loading conditions is crucial. Despite numerous fluvial studies focusing on the stability of geobags, none have specifically investigated the drag and friction forces acting on a single bag under current loading conditions. Additionally, no computational fluid dynamics (CFD) study has previously simulated the motion and movement of submerged geobags. In order to fill this knowledge gap, the present study employed a transient CFD model to simulate the movement of geobags at the bottom of the channel, utilizing the technique of Overset mesh. The image processing technique is also implemented to determine the exact edges and shape of bags before failure at the bottom of the channel. Through the simulation, the drag and friction force affecting a single geobag were determined. The effects of shape, material and filling ratio of the geobags were investigated. Ultimately, the failure velocity of geobags which follow the same shape was determined.

# Preface

This dissertation represents an independent and original work by the author, Saman Shabani. No part of this thesis has been previously published. The numerical simulations conducted in this research have been validated using data obtained by Kendra White in T. Blench Hydraulic Laboratory at the University Of Alberta.

# Acknowledgements

I would like to express my deep and sincere gratitude to all those who have supported me throughout this thesis journey. First and foremost, I am deeply indebted to my supervisors Dr. Carlos F Lange and Dr. Yuntong She, for their valuable guidance, inspiration and constant encouragement and unwavering support. I would like to thank them for being wonderful mentors and teachers to me, and I have been extremely lucky to have supervisors who care about my work.

My deepest appreciation goes to my family, especially my sister, Simin, and my brother-in-law, Ali, for their unwavering belief in my abilities and constant encouragement. Their love and support have motivated me to overcome challenges and pursue excellence.

I would like to thank you, my colleagues and members of the CFD-Lab and my friends, especially Dr. Fatemeh Razavi, for their support and help in this journey.

I would like to offer my sincere appreciation to the faculty members at The University of Alberta and the staff at the Northwest Hydraulic Consultants (NHC) company for providing an enriching academic environment and resources that have contributed to the success of this work.

I express my sincere gratitude to NSERC for providing funding for this project. Your generous contributions have provided me with the opportunity to pursue scientific endeavours. Thank you for contributing to the advancement of knowledge and innovation in this field. Lastly, I would like to express my gratitude to all the participants and individuals who contributed to this research, without whom this work would not have been possible.

# Table of Contents

<b>1</b>	<b>Introduction</b>	<b>1</b>
1.1	State of the Art Review . . . . .	3
1.1.1	Geobag Coastal Structures . . . . .	3
1.1.2	Geobag Riverbank Structures . . . . .	6
1.2	Motivation . . . . .	9
1.3	Research gap . . . . .	10
1.4	Research Objective . . . . .	11
1.5	Thesis Outline . . . . .	12
<b>2</b>	<b>Methods and Procedure</b>	<b>13</b>
2.1	Introduction . . . . .	13
2.2	Channel flume and properties of geobags in Experiment . . . . .	13
2.3	Numerical Simulation . . . . .	15
2.3.1	Image processing for edge detection using OpenCV2 . . . . .	15
2.3.2	Governing equations . . . . .	17
2.3.3	Geobag and hydrodynamic forces . . . . .	20
2.3.4	Stability of Geobag . . . . .	21
2.4	Model Implementation . . . . .	23
2.4.1	Model Geometry . . . . .	23
2.4.2	Computational setup and boundary conditions . . . . .	24
2.4.3	Verification and Validation . . . . .	30
2.5	Determining the effective-coefficient of geobag . . . . .	33
2.6	Determining Friction Coefficient . . . . .	33
<b>3</b>	<b>Results and Discussion</b>	<b>35</b>
3.1	Geometry of geobags prior to failure . . . . .	35
3.2	The friction coefficient of bags . . . . .	36
3.3	The effective coefficient of bags . . . . .	38
3.4	Effects of shape on the incipient motion of geobag . . . . .	40

3.5	Effects of material on the incipient motion of the geobag . . . . .	49
3.6	Effects of filling ratio on the incipient motion of geobag . . . . .	58
3.7	The hypothetical geobag . . . . .	65
<b>4</b>	<b>Conclusion</b>	<b>72</b>
4.1	Summary . . . . .	72
4.2	Future works . . . . .	77

# List of Tables

2.1	Material properties of geobag in the experiment . . . . .	14
2.2	Material properties of the simulated geobag . . . . .	29
3.1	The angle of friction and friction coefficient of geobag under dry and wet conditions . . . . .	37
3.2	Effective Coefficient domain for geobags . . . . .	40
3.3	Material properties of the hypothetical geobag . . . . .	65
3.4	Average of Drag and Friction force affects the hypothetical geobag .	67

# List of Figures

1.1	Maroochydore beach revetment[2] . . . . .	2
1.2	Image of sand-filled geotextile bags used for the Brahmaputra-Jamuna River in 1997 (near the Sirajganj town) [6] . . . . .	3
1.3	Sand filled geotextile container projects for shoreline protection (2009)[2] . . . . .	4
1.4	Three elements of geobags for field study in Jaumana river (2009)[4]	7
2.1	A geobag in the channel flume at the T. Blench Hydraulics Laboratory at the University of Alberta [36] . . . . .	15
2.2	Flowchart of image processing . . . . .	16
2.3	Example input image, after segmentation, and the final output . . .	17
2.4	Rectangular prism . . . . .	20
2.5	Forces acting on a submerged geobag . . . . .	20
2.6	Creating the geometry in Space Claim . . . . .	23
2.7	Schematic of the computational domain and boundary conditions . .	25
2.8	Meshing of subdomain and domain . . . . .	26
2.9	Locations of velocity profile measured upstream and on top of the cement bag . . . . .	31
2.10	Comparing the velocity profiles of experimental data vs numerical simulation of the cement bag . . . . .	32
2.11	Geobag on the inclined surface . . . . .	34
3.1	Geometry of cloth and geotextile bags used for modeling (C denotes cloth bag; G denotes geotextile bag; 1, 2, 3 indicates a fill ratio of 54%, 69%, and 84%, respectively) . . . . .	36
3.2	Effective coefficient for Geotextile bags . . . . .	41
3.3	Effective coefficient for cloth bags . . . . .	42
3.4	Pathlines of velocity magnitude at failure velocity 0.51 m/s for G1 downstream . . . . .	43
3.5	Pathlines of velocity magnitude at failure velocity 0.63 m/s for G1 even	43

3.6	Pathlines of velocity magnitude at failure velocity 0.75 m/s for G1 upstream . . . . .	44
3.7	Contour of static and total pressure at failure velocity (0.51 m/s) for G1 downstream . . . . .	45
3.8	Contour of static and total pressure at failure velocity (0.63 m/s) for G1 even . . . . .	45
3.9	Contour of static and total pressure at failure velocity (0.75 m/s) for G1 upstream . . . . .	46
3.10	Plot of the center of mass at failure velocities for G1 downstream, even, and upstream with the effective coefficient (0.27 for G1 downstream, 0.26 for G1 even, 1 for G1 upstream ) . . . . .	47
3.11	Drag and friction forces at failure velocity 0.51 m/s for G1 downstream with the effective coefficient (0.27) . . . . .	48
3.12	Drag and friction forces at failure velocity 0.63 m/s for G1 even with the effective coefficient (0.26) . . . . .	48
3.13	Drag and friction forces at failure velocity 0.75 m/s for G1 upstream with the effective coefficient (1) . . . . .	49
3.14	Contour of velocity magnitude at failure velocity (0.75 m/s) for C1 downstream . . . . .	50
3.15	Contour of velocity magnitude at failure velocity (0.51 m/s) for G1 downstream . . . . .	50
3.16	Contour of static and total pressure at failure velocity (0.75 m/s) for C1 downstream . . . . .	52
3.17	Contour of static and total pressure at failure velocity (0.51 m/s) for G1 downstream . . . . .	53
3.18	Vector plot of velocity magnitude at failure velocity of 0.75 m/s for C1 downstream . . . . .	54
3.19	Vector plot of velocity magnitude at failure velocity of 0.51 m/s for G1 downstream . . . . .	55
3.20	Plot of drag versus friction force at failure velocity 0.75 m/s for C1 downstream with the effective coefficient (0.75) . . . . .	56
3.21	Plot of drag versus friction force at failure velocity 0.51 m/s for G1 downstream with the effective coefficient (0.27) . . . . .	56
3.22	Pathlines of velocity magnitude at failure velocity 0.75 m/s for C1 downstream . . . . .	57
3.23	Pathlines of velocity magnitude at failure velocity 0.51 m/s for G1 downstream . . . . .	57

3.24	Contour of velocity magnitude at failure velocity (0.51 m/s) for G1 downstream . . . . .	59
3.25	Contour of velocity magnitude at failure velocity (0.61 m/s) for G2 downstream . . . . .	59
3.26	Contour of velocity magnitude at failure velocity (0.78 m/s) for G3 downstream . . . . .	60
3.27	Contour of static and total pressure at failure velocity (0.51 m/s) for G1 downstream . . . . .	61
3.28	Contour of static and total pressure at failure velocity (0.61 m/s) for G2 downstream . . . . .	62
3.29	Contour of static and total pressure at failure velocity (0.78 m/s) for G3 downstream . . . . .	63
3.30	Plot of the drag versus friction force at failure velocity 0.51 m/s for G1 downstream with the effective coefficient (0.27) . . . . .	64
3.31	Plot of the drag versus friction force at failure velocity 0.61 m/s for G2 downstream with the effective coefficient (0.27) . . . . .	64
3.32	Plot of the drag versus friction force at failure velocity 0.78 m/s for G3 downstream with the effective coefficient (0.27) . . . . .	65
3.33	Geometry of the hypothetical geobag . . . . .	66
3.34	Contour of static pressure at failure velocity 0.95 m/s for the hypothetical geobag . . . . .	68
3.35	Contour of total pressure at failure velocity 0.95 m/s for the hypothetical geobag . . . . .	68
3.36	Vector plots of velocity magnitude at failure velocity 0.95 m/s for the hypothetical geobag . . . . .	69
3.37	Pathlines the velocity profile at failure velocity 0.95 m/s for g1 downstream . . . . .	69
3.38	Plot of the drag and friction force versus time at a velocity lower than failure 0.9 m/s for the hypothetical geobag . . . . .	70
3.39	Plot of the drag and friction force versus time at failure velocity 0.95 m/s for the hypothetical geobag . . . . .	71

# List of Symbols

## Latin

$\delta_{ij}$	Kronecker delta
$\dot{v}_G$	Translational motion for centre of gravity
$\dot{u}$	temporal flow acceleration
$\epsilon$	Dissipation rate of turbulence
$\mu$	Molecular viscosity
$\mu_s$	Coefficient of static friction
$\rho$	Density of the fluid
$\rho_s$	Density of sand
$\rho_w$	Density of water
$\sigma_k$	Model constant
$\tau_{wall}$	Shear wall
$\vec{\omega}_B$	Angular vector of rigid body
$\vec{F}_G$	Force vector due to gravity
$\vec{M}_B$	Moment vector for the body
$a$	Length of rectangle
$A_T$	Horizontal cross-sectional area
$b$	Width of rectangle
$c$	Height
$C_{1\epsilon}, C_{2\epsilon}$	Model constant
$C_D$	Drag Coefficient
$C_L$	Lift coefficient
$C_M$	Inertia Coefficient

$F_D$	Drag force
$F_I$	Inertia force
$F_L$	Lift force
$F_W$	Weight
$g$	gravitational acceleration
$G_\epsilon$	Generation of turbulence dissipation rate
$G_k$	generation of turbulence kinematic energy due to mean velocity gradient
$k$	Turbulence kinetic energy
$L$	Inertia tensor
$m$	Mass
$r$	radius of sphere
$t$	Turbulence viscosity
$u$	Velocity
$u_*$	Friction velocity in the near wall region
$u_{\text{overturning}}$	The minimum near-bed velocity for overturning
$u_{\text{slide}}$	The minimum near-bed velocity for sliding
$u_x, u_y, u_z$	Velocity component in x, y and z direction
$V$	Volume
$y$	distance from the wall
$y^+$	y-plus
$Y_\epsilon$	dissipation of turbulence dissipation rate
$Y_k$	dissipation of turbulence kinematic energy

# Abbreviations

**6DOF** Six Degrees of Freedom.

**CFD** Computational Fluid Dynamics.

**COBRAS** Cornell Breaking Waves and Structures.

**DEM** Discrete Element Method.

**FEM** Finite Element Method.

**FSI** Fluid-structure Interactions.

**GSCs** Geotextile Sand Containers.

**k-epsilon** turbulent kinetic energy-the rate of dissipation of the turbulent kinetic energy.

**OpenCV** Open Source Computer Vision Library.

**OpenFOAM** Open-Source Open Field Operation and Manipulation.

**RANS** Reynolds Average Navier-Stokes Equations.

**RGB** Red, Green and Blue.

**UDF** User Defined Function.

**VOF** Volume Of Fluids.

# Chapter 1

## Introduction

Geobags, which are also known as geotextile sand containers, are flexible bags that are filled with sand or other materials and arranged in specific patterns, providing stability, strength, and protection against floods and erosion caused by natural disasters. Geobag is an innovative solution that has been used to manage soil erosion and control sediment in a wide range of civil engineering projects, including shorelines and riverbanks. Cost-effective, environmentally friendly and rapid mobilization during emergencies are a couple of advantages of using geobags over traditional hard material. Some of the common applications of the geobags are as follows:

1. Geobags have been used to protect shorelines, dams and harbours from erosion caused by wave loading and current loading.
2. Soil erosion is a major problem leading to deforestation, floods and loss of fertilized lands. Geobags serve as a solution to mitigate soil erosion.
3. Slopes prone to soil erosion and landslides can be stabilized using geobags.
4. Geobags play a role in restoring and preserving ecosystems that are at risk due to erosion and habitat loss.

Geobags have found extensive application along shorelines and riverbanks as a protective measure against soil erosion. Maroochyore Beach is located south of Maroochy River in southeast Queensland, Australia, which includes river and ocean frontage. In November 2000, erosion became a serious problem for Maroochyore Beach in a way that adversely affected the foreshore and caravan park during the imminent cyclonic season. As shown in Figure 1.1, non-woven geotextile units were filled and placed in the dunal system as a defence barrier. Observations showed stability higher than expected during high-wave attacks[1].



Figure 1.1: Maroochyore beach revetment[2]

The Brahmaputra River and Maroochyore Beach are an example of the application of geobags. The Brahmaputra River originates in the Himalayas, and flows through China, India, and Bangladesh, eventually entering the Bay of Bengal. The Jamuna refers to the last 250 km of the reach in Bangladesh. The bank of the river is susceptible to erosion of unconsolidated sandy soil, which, combined with floods, causes large-scale devastation in this countryside. The population of Bangladesh is over 1200 people per square kilometre, and as a result of erosion along the Jamuna and Padma rivers, an estimated 2.2 million people have been displaced since the 1970s [3]. Additionally, the continued loss of land affects the economic development

of Bangladesh and keeps the residents in poverty. As a solution to these issues, erosion protection structures consisting of geobags have been constructed to improve riverbank stability [3–5]. Figure 1.2 shows the geotextile bags utilized on the bank of the Brahmaputra River.



Figure 1.2: Image of sand-filled geotextile bags used for the Brahmaputra-Jamuna River in 1997 (near the Sirajganj town) [6]

## 1.1 State of the Art Review

The use of geobags is widespread in coastal engineering, riverbank protection, and shore protection. By creating a physical barrier, geobags prevent soil erosion and further damage to riverbanks and shorelines. The bags are usually arranged in rows along the bank, filled with sand, gravel, or other materials to create stable and erosion-proof structures. Geobags can provide long-lasting protection for the soil and reduce erosion on shorelines and riverbanks when installed appropriately.

### 1.1.1 Geobag Coastal Structures

Several studies attempted to gain a better understanding of the performance of geobag structures in coastal environments, where the wave action dominates [7–12]. Figure 1.3 shows the application of geobag for shoreline protection. Shoreline protection

studies generally fall into one of the following categories: 1) Geobag design specifications, 2) Geobag construction specifications, 3) Mechanical properties of geobags, and 4) Hydraulic forces influencing geobags. Design specification of the geobags is summarized in its materials specifications, including sand and fabric. Research conducted by Saathoff et al. [13] demonstrates that the sand with  $d_{50}$  falls within the range of 15 to 25 mm, suitable for shoreline and Bezuijen et al.[14] showed that using dry and clean sand as a filling material can reduce the risk of tearing the bags. The length of the geobags is 1.22 to 2 times the width of the bag. However, the thickness might vary as a result of the filling ratio [1, 13]. Numerous field and laboratory studies [2, 15–17] indicate that the filling ratio of 80% is the most acceptable filling ratio among coastal protection owing to its superior stability performance.



Figure 1.3: Sand filled geotextile container projects for shoreline protection (2009)[2]

Construction specification of geobags coastal structures is primarily focused on the thickness of the protection work, geobag placement, and structural slope, which affect the failure mechanism of geobags. The failure mechanism needs to define the concept of the incipient motion of geobags. Pilarczyk explained the concept of "incipient velocity" of geobag, which is defined as the velocity required to initiate the movement of geobag revetments. Shirlal and Mallidi [18] conducted a physical model to determine

the stability of a submerged reef constructed from GSC in three distinct alignments: parallel, perpendicular, and flemish. The parallel alignment, when utilizing two layers of geotextiles, emerged as the only stable configuration among these three. Another pivotal construction parameter is geobag structure slope. According to the available studies, the most commonly used slope for coastal applications are 1V:1H, and 1V:2H [7, 19–21], but, the slope can vary depending on the design wave height and erosion pattern [22].

Mechanical properties play a crucial role in the stability of the geobags. Permeability, deformation and internal friction are the most important mechanical properties of geobags. The deformation and permeability of the geotextile sand containers were investigated by Recio and Oumeraci [23]. Their findings indicate that the total forces and moments that affect the geobags displacement depend on the wave propagation inside the internal gaps between the geobags. Additionally, the deformation of geotextile sand bags happens in the latter part of the bags due to the accumulation of the sand in the seaward end of the bags, leading to a reduction in contact area with neighboring bags. The angle of friction is another significant parameter for studying the mechanical properties of geobags. Kim et al., and Krahn et al. [24, 25], utilizing large shear boxes to ascertain friction angles under varying loads, determined that the average angle of friction was  $30^\circ$ .

The hydraulic forces that affect the stability of geobags were investigated by Kim et al., Pilarczyk et al., and Recio and Oumeraci [21, 24, 26]. Failure occurs due to inertia, drag and lift forces affecting the geobags. According to studies, overlapping, sliding, puncturing, pullout, and toe scour are the most common modes of failure in coastal applications [16, 27, 28]. Recio and Oumeraci [23] conducted laboratory tests to investigate hydrodynamic forces, specifically focusing on drag and lift effects. They determined the drag and lift coefficients associated with these forces. Their study indicates a uniform lift coefficient across bags positioned at the top, middle, and bottom of the geobags structure. However, large variations were observed for the

drag coefficients, which ranged from 4 to 15 for top bags, 2.5 to 9 for middle bags, and 0.5 to 3 for bottom bags.

A couple of studies investigated the mechanical and hydrodynamic properties that affect the geobags. Among these studies, the only published numerical study focused on determining the hydrodynamic and frictional forces that affect the geobags is done by Recio and Oumeraci [21]. Recio and Oumeraci's study utilized the "COBRAS-UDEC," which is a RANS-VOF model based on Reynolds-Averaged Navier-Stokes equations and Volume Of Fluids to represent the displacement of the geobags with three different angles of friction  $8^\circ$ ,  $18^\circ$  and  $28^\circ$ . Their finding shows that larger displacement is for smaller angles of friction. Nonetheless, additional numerical research is necessary to comprehensively determine the impact of hydrodynamic forces affecting the geobag.

### **1.1.2 Geobag Riverbank Structures**

Coastal studies provide some insight in terms of geobags' physical and mechanical properties. However, due to differences in hydraulic loading, coastal-based studies where wave action is prevalent cannot be used to determine how geobag performs in riverbank revetments.

Riverbank revetments in the Brahmaputra river in Bangladesh consist of three main components, as shown in Figure 1.4 [4]:

- i) The slope protection area under water, which helps to prevent riverbank erosion
- ii) The slope protection, as is above a low water level, to prevent current erosion and wave erosion during flood seasons.
- iii) Toe protection by means of falling aprons to prevent riverbed scouring from undermining slope protection.

Determining the stable slope for geotextile sand containers investigated by NHC for the Brahmaputra River in Bangladesh, [29]. The stable slope needs to be started underwater to reduce the load on the bank and increase the safety factor for the

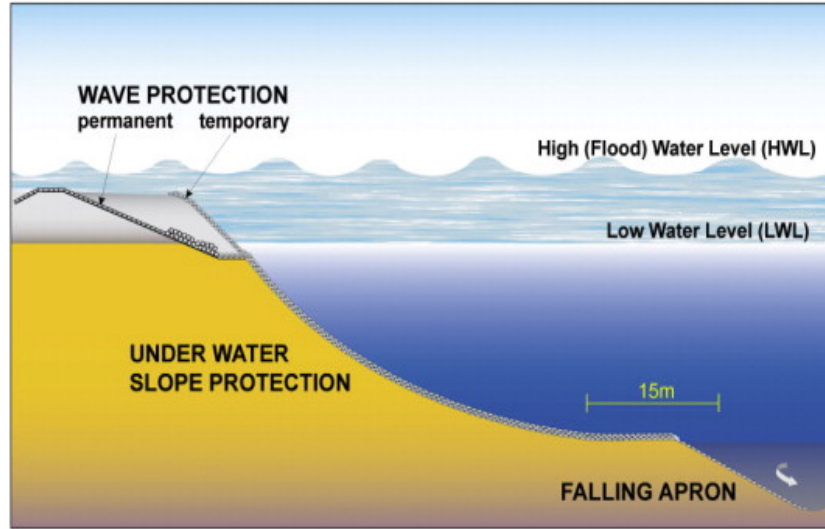


Figure 1.4: Three elements of geobags for field study in Jaumana river (2009)[4]

stability of the slope. Initially, geobags are dumped along the shoreline and shallow section of the riverbank in a massive heap, which self-launches into deeper water. This ‘falling apron’ enables better protection against toe scouring and typically launches to a geotechnically stable slope of 1V:2H (V = vertical, H =horizontal). The falling apron is a key component of the geobag revetment structure design, as sections of the rivers are too deep to allow for direct placement of the geobags. According to the findings of this experiment, the optimal stable slope for underwater areas is 1V:2H. The required slope for concrete blocks, however, is 1V:5H, which is not stable for geotextile bags[4]. Other revetment configuration studies concentrated on redirecting the fluid flow and maintaining the desired water depth to protect the riverbanks from erosion [30, 31]. The redirecting main flow studies can be categorized into three different groups, namely, porcupine, geobag, and a combination of porcupine and geobag (hybrid). Oberhargemann [4], Aamir and Sharma [32] revealed that the implementation of both porcupine and geobag layouts led to notable reductions in flow velocity and encouraged sediment deposition. However, the design of training works needs to be tested before deploying in large rivers. Several researchers used numerical river models to overcome the limitations of river training work studies. Gao et al. [33]

utilized a 3D-dimensional hydrodynamic model developed in Ansys Fluent to model concrete tetrahedral frame revetments. Kakati et al. [34] used the three-dimensional hydrodynamic open-source Open Field Operation and Manipulation (OpenFOAM) for modeling the geobag and porcupine structures. The numerical model was employed to assess three types of structures: the porcupine screen, the geobag screen, and a hybrid layout. From these analyses, it became evident that the hybrid layout exhibited a more effective reduction in velocity compared to the geobags. However, this study did not model the movement of geobag in the flow field. Further research needs to be done to explore the onset of geobag motion under various flow conditions.

The study of geobag failure mechanisms primarily focused on the examination of the filling ratio of geobags and the hydrodynamic forces influencing these bags. It appears that geobags with an optimal fill ratio demonstrate greater stability. Thompson et al. [35] found that the stability of geobag is a function of the filling percentage and flexibility of geobags. They proposed a different value for the "stability coefficient," which is influenced by both the filling ratio and flexibility of geobags. Geobags with a higher stability coefficient show less stability. Their study showed that the sandbags with a filling ratio of 84% to 95% exhibit the highest stability, and the stability coefficient for the filling ratio above 80% is considered 0.07. Analyzing the failure mechanism of geobags also required understanding the impact of hydrodynamic forces on these structures. Pilarczyk [26] defined the failure or incipient motion of geobags when the lift, drag and inertia force exceeds the contact and cohesion forces and weight of the submerged elements. A couple of studies focused on determining the drag and lift forces affecting a group of geobags. Zhu et al. [20] conducted a laboratory investigation to study the incipient motion of the sandbag dike located in the lower reach of the Changjiang River. The sandbags were placed in the channel bed in two configurations: parallel and perpendicular to the flow direction. The results indicate that the lift coefficient approaches zero for both configurations, indicating the negligible role of lift force in initiating the motion of the sandbags. White [36]

examined the stability of individual geobags under different fill ratios, bag materials, and shapes, considering both flat and sloped beds. According to their study, geobags with higher fill ratios and more flexibility demonstrated improved levels of stability. Additionally, the material of the geobags was examined by comparing the geotextile and cloth bags throughout the experiment. The geotextile bags indicated a consistent shape progression during the test, and a clear trend was observed for failure velocities when considering the initial shape of the bags. The cloth bags, However, exhibited a lack of definitive pattern in their shape progression due to inherent variability. Thompson et al. [37] used Computational Fluid dynamics (CFD) to determine the hydrodynamic forces that affect the geobags. According to this study, the drag coefficient for multiple geobags was found to be 0.02. Their study did not quantify the lift force, as the model did not replicate the conditions beneath the geobags. Akter et al. investigated the failure mode of geotextile sand containers on the riverbank with the laboratory experiment and the Discrete element method (DEM)[38, 39]. The critical velocity was determined through the experiment to use in a DEM simulation. With the DEM model, the drag coefficient and lift coefficient were found to be 0.5 and 0.8, respectively, which are the average drag and lift coefficients for all geobags.

## 1.2 Motivation

Riverbank erosion is one of the major environmental issues in different parts of the world, and there is an urgent need to mitigate the problem. Geobag containers filled with sand or other materials are known to be an effective method for protecting the riverbank and shorelines from erosion due to their flexibility and being economically friendly. Nevertheless, geobags are not well understood in terms of their design and performance under various hydraulic conditions, and better modeling and optimization tools are needed to improve their efficiency.

Computational Fluid Dynamics (CFD) is a powerful tool for simulating fluid flow and predicting forces and pressures acting on structures. A numerical model of geobag

behaviour using CFD provides a method for studying fluid-structure interactions and evaluating different geobag configurations under various flow conditions. Engineers and researchers can benefit from this information to better understand geobags and optimize their designs. Such a study can help develop more effective and sustainable solutions for riverbank and shoreline protection, which are crucial for alleviating the impacts of erosion and floods.

### **1.3 Research gap**

Numerous investigations focused on the stability and failure mechanism of geobags. However, a notable gap exists in research specifically targeting the stability of individual geobags under current loading. None of these studies have addressed the determination of drag and friction forces exerted on a geobag under current loading. The drag force is generated by the interaction and contact of the geobag with a fluid flow. Friction is the resistance to relative motion between geobag, fluid layers, and the bottom of the channel sliding against each other. Additionally, no CFD studies have determined the motion and movement of geobags. While a few studies have employed the overset and dynamic mesh technique to simulate the movement of solid objects within channels [40, 41], no CFD study has yet applied the overset mesh approach to model the motion and movement of geobags. The overset mesh combines two different meshing forms in a CFD simulation and allows different zones to move relative to each other while maintaining mesh quality.

To bridge this gap in existing research, this study employs a transient three-dimensional (3-D) CFD model to comprehensively analyze the drag and friction forces influencing a single geobag located at the bottom of the channel. The utilization of an overset and dynamic mesh ensures an accurate representation of the motion of a geobag. Furthermore, since the deformation underflow cannot yet be numerically predicted, the image processing technique is implemented to precisely capture the shape of the geobag before failure for effective CFD modeling. This study provides

the details of the numerical simulation process, facilitating an exploration into geobag behaviour under current loading. Finally, the results and conclusions of the current investigation are provided.

## 1.4 Research Objective

The objective of this thesis is to employ a transient three-dimensional (3-D) Computational Fluid Dynamics (CFD) model to simulate the motion and movement of geobag using dynamic and/or overset mesh. This study analyzes hydrodynamic forces affecting the geobag and examines flow characteristics around the geobag. The specific research objectives include:

- 1. Development of a valid CFD Model:** First aim is to create a transient three-dimensional CFD model which is able to accurately simulate the fluid dynamics near and around the geobags for the riverbank applications. This model is validated with experimental study to ensure the accuracy and reliability of the model.
- 2. Determining the shape of the geobag with image processing:** The shape of the bag plays a crucial role in the onset of movement of the geobag. The objective is to specify the exact shape of the geobag before failure and utilize that image to create the corresponding model geometry.
- 3. Study of the velocity and flow pattern:** Examine the velocity distribution around the geobag and flow patterns at various flow rates. To analyze the boundary layer and velocity profile for all geobags, two different flow rates are investigated before the failure of the geobag and after the failure of the geobag. Additionally, flow separation and any recirculation zone could be identified by analyzing the contours of the velocity around the bags.
- 4. Determining the hydrodynamic forces on the geobag:** Hydrodynamic forces of the geobag, including drag and lift force, can be evaluated with CFD modeling of flow around the bag. Additionally, the drag and lift coefficient for all bags can be achieved.

**5. Determining the friction coefficient and friction force:** The friction coefficient on geobags with different fabrics will be measured with an experimental test, and then, the objective is to determine the friction force for each geobag, which prevents the onset of the movement.

**7. Model the movement of each geobag with dynamic and/or overset mesh:** Develop a CFD model using dynamic and/or overset mesh to model the onset of movement of a geobag in the channel. Additionally, a 6DOF solver was used to determine the center of mass of geobag at each time-step of the simulation to measure the movement of geobag.

## 1.5 Thesis Outline

A brief overview of the contents of the different chapters of this thesis is presented in this section.

Chapter 1, provides a general introduction to the research and describes different applications of the geobag. Additionally, the motivation behind this research is presented. This chapter provides a comprehensive overview of literature published on the study of geobag for riverbank and coastal application. The research gaps and the objective of the project are identified in this chapter.

Chapter 2, discusses the configuration of a transient three-dimensional CFD model of a geobag in a laboratory channel. The details of the modeling and meshing method are explained.

Chapter 3 offers a detailed breakdown of the drag and friction forces acting on individual geobags at each time step of the transient simulation. The forces acting on a geobag at failure are shown. The movement and motion of geobag are presented, and the effects of different factors, including the shape of the bag, filling ratio, material and velocity, on the incipient motion of geobag are provided.

Chapter 4, discusses the main conclusion of the present study and suggests recommendations for future works.

# Chapter 2

## Methods and Procedure

### 2.1 Introduction

Computational Fluid Dynamics (CFD) modeling is a cost-effective solution and valuable tool for analyzing the performance of many fluid flow problems. In this thesis, advanced techniques of modelling were used to model and analyze the performance of geobags used in the riverbank protection structures. With CFD modeling, geobag simulation can reduce the time and cost associated with physical testing and trial-and-error design. Additionally, CFD modeling can potentially help engineers and designers gain a better understanding of complex fluid-structure interaction and develop more effective solutions. This chapter describes the different steps involved in CFD modeling of geobags, which includes Image processing of geobags, 3D modeling of geobags, defining the boundary conditions, and mesh generation. Additionally, the dynamic mesh techniques utilized in this simulation are highlighted in this chapter. Finally, the experimental part of this study, which involves determining the friction coefficient of geobags is also provided at the end of this chapter.

### 2.2 Channel flume and properties of geobags in Experiment

The current study utilized data and findings from a previous laboratory investigation conducted by White [36]. The experiments were conducted in a long recirculating

flume 1.2 m wide and 25 m long, located at the T. Blench Hydraulics Laboratory at the University of Alberta as shown in Figure 2.1. The sidewalls of the channel were made of glass, and the bed was roofing asphalt (Manning’s  $n = 0.0016$ ). The flow depth was 0.3 m, and the slope of the bed was zero. The flow depth was measured with a point gauge with an accuracy of  $\pm 0.5$  mm. 9 cloth bags and 9 geotextile bags with varying fill ratios and different initial shapes were studied. Table 2.1 provides detailed characteristics of all the geobags utilized in this investigation. The fill ratio is calculated by dividing the actual mass of the geobag by its mass when fully filled with sand. The density, thickness and mass mentioned in the Table were measured for the geobags.

Table 2.1: Material properties of geobag in the experiment

Name	Material	Initial shape	Fill ratio%	Density of geobag (kg/m <sup>3</sup> )	Thickness of geobag (m)	Mass (kg)
C1	Cloth	Downstream	54	1716	0.014	0.234
	Cloth	Even	54	1716	0.014	0.234
	Cloth	Upstream	54	1716	0.014	0.234
C2	Cloth	Downstream	69	1628	0.015	0.299
	Cloth	Even	69	1628	0.015	0.299
	Cloth	Upstream	69	1628	0.015	0.299
C3	Cloth	Downstream	84	1788	0.022	0.364
	Cloth	Even	84	1788	0.022	0.364
	Cloth	Upstream	84	1788	0.022	0.364
G1	Geotextile	Downstream	54	1609	0.017	0.234
	Geotextile	Even	54	1609	0.017	0.234
	Geotextile	Upstream	54	1609	0.017	0.234
G2	Geotextile	Downstream	69	1807	0.021	0.299
	Geotextile	Even	69	1807	0.021	0.299
	Geotextile	Upstream	69	1807	0.021	0.299
G3	Geotextile	Downstream	84	1804	0.025	0.364
	Geotextile	Even	84	1804	0.025	0.364
	Geotextile	Upstream	84	1804	0.025	0.364



Figure 2.1: A geobag in the channel flume at the T. Blench Hydraulics Laboratory at the University of Alberta [36]

## 2.3 Numerical Simulation

### 2.3.1 Image processing for edge detection using OpenCV2

Previous studies [36] showed that the shape of the geobag can greatly affect its stability. As the deformation of the geobag is not modeled, it is crucial to determine the shape of the geobag prior to failure before modeling it in ANSYS Fluent. This was achieved by using image processing techniques to extract the edges and shape of the submerged geobag from the images taken in the laboratory experiments by White [36]. OpenCV2 is an applicable library that focuses more on real-time applications [42]. This library is officially written for the C++ language; but, it is also available for Python. In this study, OpenCV2 was used as a machine-learning package to analyze image patterns of geobags in Python. The images were processed to determine the borders of the geobag for simulation with Ansys Fluent. This process makes the objects more clearly visible and fills the small holes in the objects. Figure 2.2 shows the different steps of image processing of geobags in the context of this research.

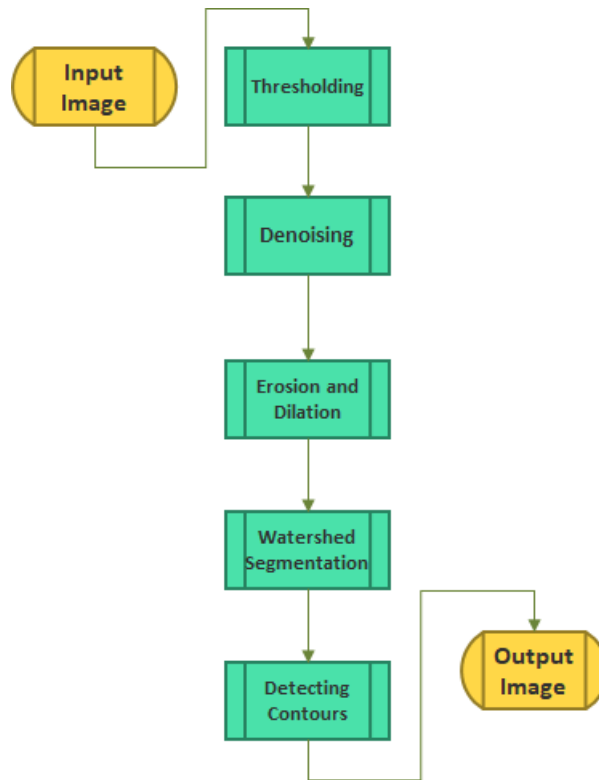
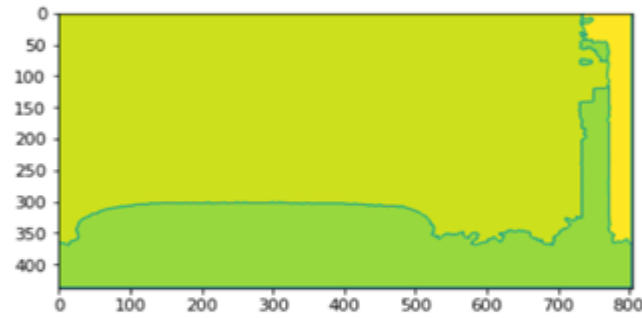


Figure 2.2: Flowchart of image processing

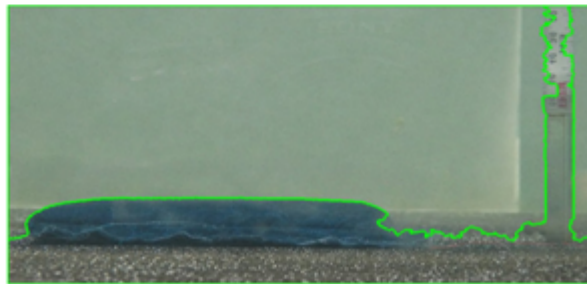
The input image is in the RGB form. Thresholding, which is a type of image segmentation that changes the pixel of the image to make it easier to analyze, converts the image from RGB colour into a binary image that is simply black and white. This is a way to select areas of interest in the image and ignore the parts that are not of concern. In the denoising step, the background noise is removed while the edges remain, helping to reveal a smoother image. The next step is erosion and dilation. Dilation means adding pixels to the boundary of the image to make the boundary more visible, while erosion removes excessive pixels from some boundaries of the image. The number of added or removed pixels from the image depends on the shape and size of the structuring element used in the image processing. Figure 2.3 shows an example input image, after segmentation, and the final output.



a) Geobag at the bottom of the channel



b) Watershed segmentation



c) The final output of the image

Figure 2.3: Example input image, after segmentation, and the final output

### 2.3.2 Governing equations

CFD simulation solves the partial differential equations governing the fluid flows. Calculations are based on mass, momentum, and energy balance from fundamental fluid dynamics. CFD solves the equations iteratively, resulting in overall residuals. A residual is the sum of the imbalances of all the computation cells for a general variable, which is related to the numerical error in the discretized equations. Convergence is determined by summing the error in all control volumes and overall discretized equations. In this simulation, the fluid is assumed to be continuous, and velocity,

density, pressure, etc., are described as macroscopic properties.

The 3D continuity equation for an incompressible fluid is as follows:

$$\operatorname{div} \vec{V} = 0 \quad (2.1)$$

The following equation represents the conservation of momentum equations for turbulence flow, the so-called Reynolds Averaged Navier-Stokes (RANS) equations. During the process of Reynolds averaging, an extra stress tensor, known as Reynolds Stress, emerges. In order to solve the RANS equations, it becomes necessary to express the Reynolds stress tensor in relation to the mean flow properties.

$$\frac{\partial(\rho u_i)}{\partial t} + \frac{\partial(\rho u_i u_j)}{\partial x_j} = -\frac{\partial P}{\partial x_i} + \frac{\partial}{\partial x_j} \left[ \mu \left( \frac{\partial u_i}{\partial x_j} + \frac{\partial u_j}{\partial x_i} - \frac{2}{3} \delta_{ij} \frac{\partial u_k}{\partial x_k} \right) \right] + \frac{\partial}{\partial x_i} (-\rho \overline{u'_i u'_j}) \quad (2.2)$$

$\overline{u'_i u'_j}$  is defined as the Reynolds stress tensor and represents the fluctuation of the velocity field. The incorporation of this non-linear Reynolds stress term required further modeling to complete the RANS equations for the solution. As a result, numerous turbulence models have been developed.

The widely used K-epsilon turbulence model is used in this study. The turbulence kinetic energy,  $k$ , and its rate of dissipation,  $\epsilon$ , are calculated from the following equations:

$$\frac{\partial}{\partial t}(\rho k) + \frac{\partial}{\partial x_i}(\rho k u_i) = \frac{\partial}{\partial x_i} \left[ \left( \mu + \frac{\mu_t}{\sigma_k} \right) \frac{\partial k}{\partial x_j} \right] + G_k + G_b - \rho \epsilon - Y_M + S_k \quad (2.3)$$

$$\frac{\partial}{\partial t}(\rho \epsilon) + \frac{\partial}{\partial x_i}(\rho \epsilon u_i) = \frac{\partial}{\partial x_j} \left[ \left( \mu + \frac{\mu_t}{\sigma_\epsilon} \right) \frac{\partial \epsilon}{\partial x_j} \right] + C_{1\epsilon} \frac{\partial \epsilon}{\partial x_j} (G_k + C_{3\epsilon} G_b) - C_{2\epsilon} \rho \frac{\epsilon^2}{k} + S_\epsilon \quad (2.4)$$

In these equations,  $\rho$  is the density of the fluid,  $k$  is the turbulence kinetic energy,  $\mu_t$  is the turbulence viscosity,  $u$  is the velocity component in the  $x$  direction,  $\mu$  is the molecular viscosity,  $\sigma_k$  is a model constant,  $\epsilon$  is the turbulent dissipation rate,  $\delta_{ij}$

is the Kronecker delta,  $G_k$  is defined as the generation of turbulence kinetic energy due to mean velocity gradients,  $Y_M$  is the dissipation of turbulence kinetic energy,  $C_{1\epsilon}$  and  $C_{2\epsilon}$  are model constants,  $G_\epsilon$  is the generation of turbulence dissipation rate,  $Y_\epsilon$ ,  $S_\epsilon$ ,  $S_k$ ,  $G_b$  is the dissipation of turbulence dissipation rate, user-defined source, user-defined source and production of TKE due to buoyancy, respectively.

The Six Degree Of Freedom (6DOF) solver solves the equation of motion for solid bodies in addition to the Navier-Stokes equation for the fluid flows. This solver determines the forces and moments acting on the rigid body due to fluid flow. The forces and moments are used to calculate the translational and angular motion of the center of mass for the object. Using equations of motion, the 6DOF solver calculates translation and rotation of the object. In this equation, the reference point is situated at the bottom-left corner of the geobag. The equations of motion for a solid body in the fluid are as follows[43]:

$$\dot{\vec{v}}_G = \frac{1}{m} \sum \vec{f}_G \quad (2.5)$$

In this equation,  $\dot{\vec{v}}_G$  is the translational acceleration which is for the center of gravity,  $m$  is the mass, and  $\vec{f}_G$  is the force vector acting on the center of gravity.

$$\dot{\vec{\omega}}_B = \mathbf{L}^{-1}(\sum \vec{M}_B - \vec{\omega}_B \times \mathbf{L}\vec{\omega}_B) \quad (2.6)$$

where  $\dot{\vec{\omega}}_B$  and  $\vec{M}_B$  are the angular motion of the object and the moment vector for the body,  $\mathbf{L}$  is the inertia tensor, and  $\vec{\omega}_B$  is defined as angular acceleration vector of the rigid body.

Determining the center of mass and mass moment of inertia is necessary to obtain the correct simulation result. The mass moment of inertia for a rectangular prism, as shown in Figure 2.4, is calculated from the following formulas:

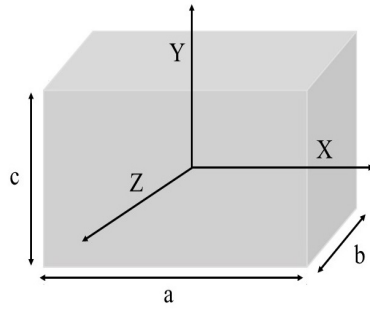


Figure 2.4: Rectangular prism

$$\begin{bmatrix} \frac{1}{12}m(a^2 + b^2) & 0 & 0 \\ 0 & \frac{1}{12}m(b^2 + c^2) & 0 \\ 0 & 0 & \frac{1}{12}m(c^2 + a^2) \end{bmatrix} \quad (2.7)$$

Geobags modelled in this thesis do not have symmetrical shapes. The Ansys Mechanical model and Ansys Fluent were used to determine the actual center of mass and mass moment of inertia for the bags.

### 2.3.3 Geobag and hydrodynamic forces

CFD was used primarily to model the stability of the submerged geobags. This study evaluated the hydrodynamic forces acting on the geobag, namely, drag, buoyancy, and lift force. The drag, inertia, and lift forces were calculated by the Ansys Fluent. Figure 2.5 shows the diagram of forces acting on the submerged geobag.

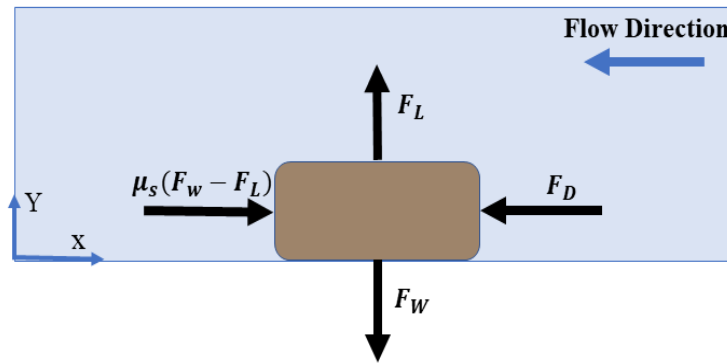


Figure 2.5: Forces acting on a submerged geobag

The drag force is calculated from the following formula:

$$F_D = \frac{1}{2}C_D\rho_w A_s u^2 \quad (2.8)$$

Where  $\rho_w$  is the density of water,  $C_D$  is the dimensionless coefficient of drag,  $u$  is the mean flow velocity, and  $A_s$  is cross-sectional area normal to the flow [9].

Where  $C_M$  is the inertia coefficient and  $V$  is the volume of geobag and  $\dot{u}$  is the flow acceleration  $\left(\frac{\partial u}{\partial t}\right)$ .

The lift force is calculated according to the following formula:

$$F_L = \frac{1}{2}C_L\rho_w A_T u^2 \quad (2.9)$$

Where  $C_L$  is the dimensionless lift coefficient,  $A_T$  is the horizontal cross-sectional area of the geobag. The drag and lift forces are calculated based on the pressure differences and viscous shear forces acting on the surface of the geobag by Ansys Fluent. The weight force is caused by the weight of the geobag under buoyancy, which is determined from the following formula:

$$F_w = (\rho_s - \rho_w)Vg \quad (2.10)$$

Where  $V$  is the volume and  $\rho_s$  is the density of geobag, respectively.

### 2.3.4 Stability of Geobag

Two modes of failure must be considered in the study of the stability of the geobags [44, 45].

Sliding occurs when

$$F_D > \mu_s(F_w - F_L) \quad (2.11)$$

Where  $\mu_s$  is the coefficient of static friction, which was determined in this study with a simple experiment that will be discussed in section 3. The minimum depth-averaged velocity for sliding ( $u_{slide}$ ) can be computed from the following formula [46]. As this study exclusively examined the sliding mode of failure, the term ( $u_{slide}$ ) represents the failure velocity of the geobag:

$$\frac{1}{2}C_D\rho_w A_T u_{slide}^2 > \mu_s F_w - \mu_s \left(\frac{1}{2}C_L\rho_w A_L u_{slide}^2\right) \quad (2.12)$$

$$\frac{1}{2} \times C_D\rho_w A_T u_{slide}^2 + \mu_s \left(\frac{1}{2}C_L\rho_w A_L u_{slide}^2\right) > \mu_s F_w \quad (2.13)$$

$$u_{slide} = \sqrt{\frac{\mu_s F_w}{0.5\rho_f(C_D A_T + C_L A_L \mu_s)}} \quad (2.14)$$

Overturning occurs when the sum of the drag, and lift force moments exceed the gravitational moments[46]

$$F_D L_D + F_L L_L > F_W L_W \quad (2.15)$$

Where  $L_D, L_L, L_W$  are the moment arms of the drag, lift, and gravitational forces. Then, the minimum depth-averaged velocity for geobag for overturning is determined from the following formula:

$$\frac{1}{2}C_D s \rho_w A_T u_{overturning}^2 L_D + \frac{1}{2}C_L \rho_w A_L u_{overturning}^2 L_L > F_W L_W \quad (2.16)$$

$$u_{overturning} = \sqrt{\frac{F_W L_W}{0.5\rho_f(C_D A_T L_D + C_L A_L L_L)}} \quad (2.17)$$

## 2.4 Model Implementation

### 2.4.1 Model Geometry

After the edges and borders of a geobag were generated by image processing, the image was imported to Ansys Space Claim software to create the geometry for simulation. Figure 2.6 shows how the geometry is created in the space claim software. This study considered two different materials, cloth, and geotextile bags, and three filling ratios 54%, 69%, and 84%, three initial shapes, upstream heavy, even, and downstream heavy, with the same dimensions (10 cm x 15 cm). Therefore, eighteen images were imported into Space Claim to create geometries of submerged geobags.

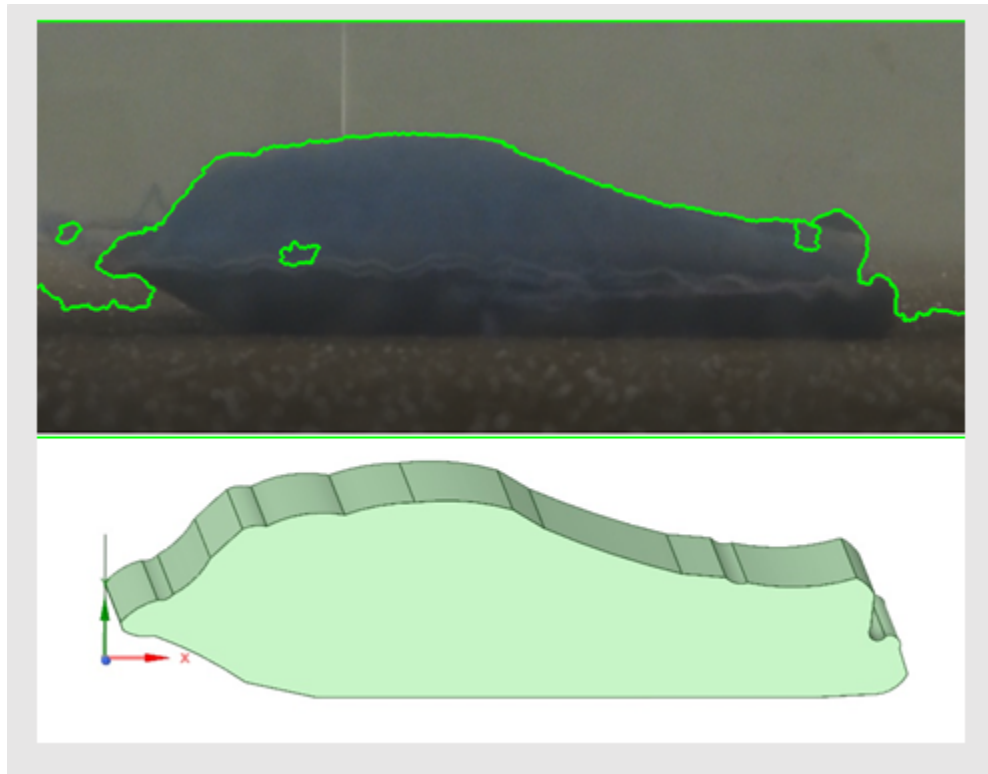


Figure 2.6: Creating the geometry in Space Claim

For this modelling, the geometry is approximated by extruding the cross-section. This is because we only had the side-view photos of the geobags. It is a simplified model with a bigger volume than the real geobag. Therefore, two different cases can be considered for the modelling of geobag.

The first case is to consider the same density as the experimental study. With a bigger volume caused by the extrusion, the mass of the geobag is larger than in the experimental study. As a result, the bag will start moving at a higher flow velocity compared to the failure velocity determined in the experimental study.

The second case is to consider the same mass as the experimental study. In this case, since the volume is larger than in the experimental case, it is required to decrease the density to arrive at the same mass. In this way, the bag will start moving at the same flow velocity as that in the experimental study. Therefore, for this study, the mass of geobags is the same as in the experimental study.

## **2.4.2 Computational setup and boundary conditions**

Figure 2.7 shows the computational domain and boundary conditions of the 3D geometry. The geobag is located at a 1cm distance from the bottom of the channel. This is because the overset mesh needs to be at least four layers of mesh distance between the geobag and the wall. The domain size was tested to ensure that the smallest changes in flow around the geobag will be captured. In addition, the effects of sides and top boundaries on the geobag were minimized by domain independence analysis. The two side walls and the top of the domain were considered zero-shear walls since only part of the channel was modelled. Dynamic mesh and overset mesh were explored for this study.

### **a) Dynamic mesh**

Dynamic mesh setting in Ansys Fluent consists of three meshing methods and four options. Three different methods include smoothing, layering, and re-meshing. Selecting the correct dynamic mesh methods and options is essential for avoiding negative volume errors in Ansys Fluent. The layering method adds or removes layers of cells based on the height of the cells and only works for structured meshes. The smoothing method allows cells of the mesh to stretch and contract. All deforming zones

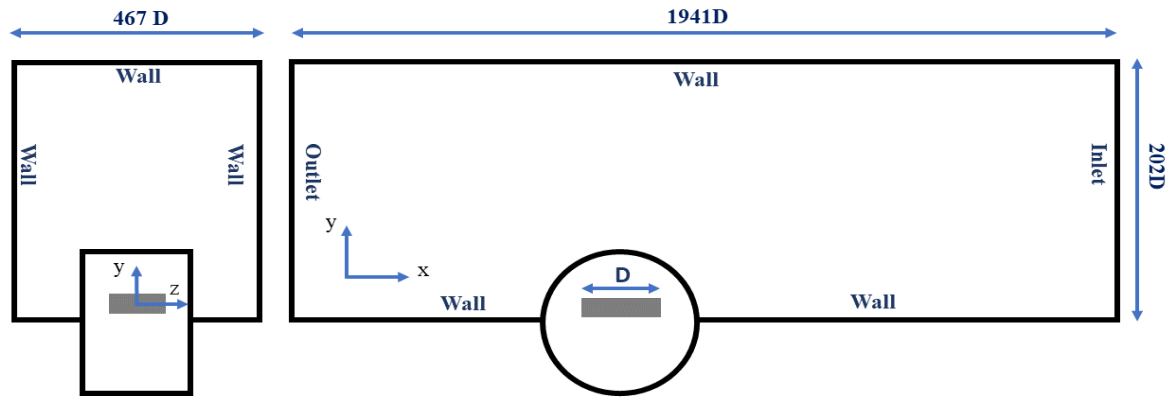


Figure 2.7: Schematic of the computational domain and boundary conditions

with dynamic boundaries can be modeled with this method, and it is most suitable for tetrahedral cells. However, the smoothing method is not appropriate for large deforming boundaries, which are used in this simulation. The last method is re-meshing, which works by the desired level of skewness. Skewness is the ratio of the length of the longest edge of an element to the minimum length between two opposite faces of the element. During the re-meshing process, the software checks the skewness of elements for the new mesh. If the skewness of the new mesh exceeded the maximum allowable value, the re-meshing process started to improve the quality of the mesh. The problem with this method is that the quality of the mesh, especially within the boundary layer, decreases significantly. Therefore, the re-meshing method is not applicable to the modeling of this simulation. The other CFD software of Ansys, CFX, was also considered for this study but only offers the re-meshing method of dynamic mesh, which always diverged in tests. For this reason, CFX was rejected in favor of Fluent, which offers the overset mesh method. An overset mesh allows large relative motion between different components and moves the layers without deforming the mesh.

## b) Overset mesh

Overset mesh, which is also known as Chimera mesh, is a technique in Ansys Fluent that allows the simulation of complex fluid-structure interactions in which one or more objects move around the surrounding fluid. Each overset mesh comprises two main parts; The first one is the background mesh, which is static mesh and covers the entire domain and cannot be moved. The second part is the component mesh, which could be one or more objects meshed independently. The component mesh is the dynamic part of the mesh, and, in this study, it consists of the subdomain and the geobag. The spatial grid comprises an inhomogeneous grid with finer mesh around the geobag and bottom of the channel and a coarser mesh close to the other domain boundaries. The component mesh (geobag and subdomain) is an unstructured grid generated with Ansys Meshing, and the background mesh is a structured grid created with Ansys ICEM. Figure 2.8 shows the meshing of the flow domain.

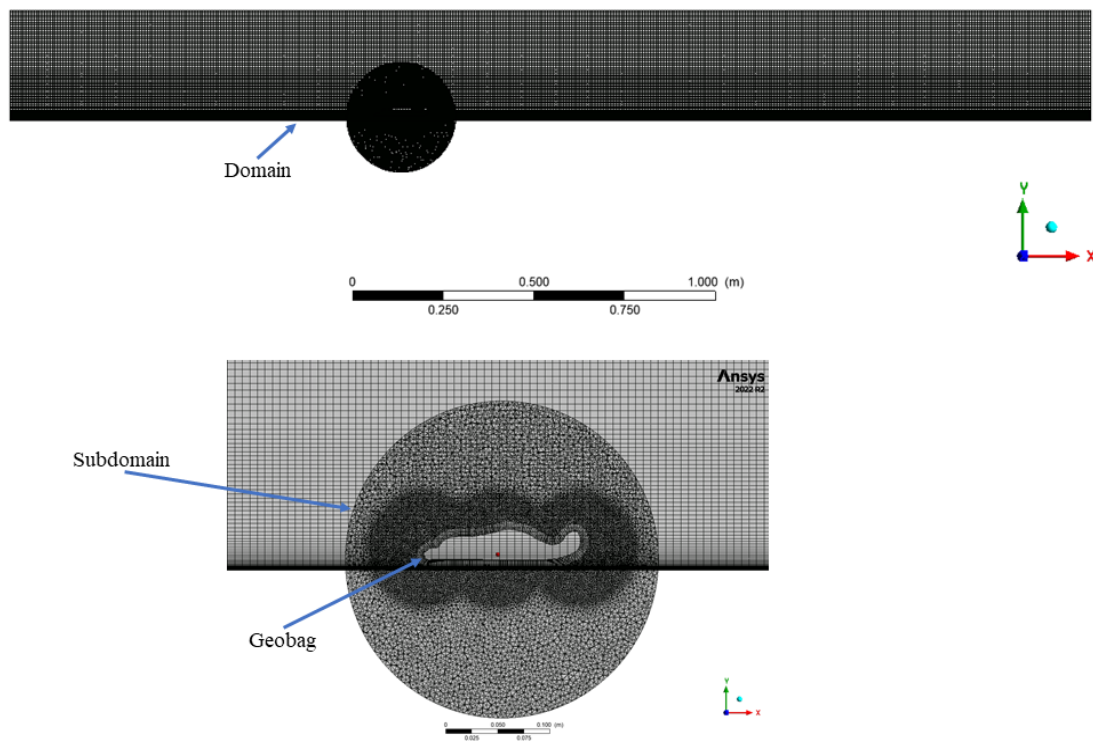


Figure 2.8: Meshing of subdomain and domain

For this simulation, only overset mesh with 6DOF and Implicit Update was used in the dynamic mesh menu to model the geobag in the channel. The details of the 6DOF option are mentioned in part d of section 2.4.2. The implicit update is an algorithm in which the deformation is accounted for implicitly by solving the governing equations without calculating the boundary motion explicitly. This approach helps to avoid re-meshing. The mesh is updated based on velocity and acceleration and the boundary motion. The governing equations for the next time step are solved based on the new mesh. The implicit update helps to maintain the quality of the boundary layer mesh during the simulation.

### **c) Solver Setting**

The numerical models were created using Ansys Fluent. The software solves 3D RANS, which resolves mass and momentum transfer. For this study, a transient solver is chosen to numerically simulate the movement of the submerged geobag. The pressure-based solver has been used with a wide range of flow velocities from 0.44 to 1.06 m/s. The motion of the component mesh can be defined with boundary profiles or user-defined functions.

### **d) User-defined function and 6DOF properties**

The 6DOF solver, based on the flow around the geobag and the geobag properties, moves the dynamic zone to the next time step. Two macros were used in the 6DOF solver to simulate the geobag at the bottom of the channel. This was achieved through the user-defined function (UDF). A UDF is a function that can be dynamically loaded with the Ansys Fluent solver, enhancing the standard features of the code [47]. For this study, two different UDFs have been used with the 6DOF solver. First, the 6DOF solver required the definition of desired properties with UDF, which comprise mass, moments, products of inertia, external forces and moments, and the body constraints. The DEFINE-SDOF-PROPERTIES macro was used to define various properties of

the geobag for the 6DOF solver. These properties include mass, mass moment of inertia, and friction force. This macro works best to simulate a solid body in the flow field.

The second UDF is the DEFINE-CONTACT macro, which was used to determine the response to a contact detection in the Ansys Fluent. Contact detection was used to identify component mesh that will have contact with the other surfaces in the background mesh. Without contact detection, the bag in the component mesh simply crosses the boundary wall in the background mesh. After the simulation starts, the geobag moves downward due to the weight of the bag and stops at the threshold distance, which is defined as the same distance (1 cm from the bottom of the channel), then moves in the direction of the flow depending on the momentum exchange between the geobag and the fluid. It is worth mentioning that there is a thin layer of fluid between the bag and the bottom of channel. In the context of Ansys Fluent, a potential solution to address this interaction is to establish a porous medium at the contact zone. This approach effectively restricts fluid movement within this specific region, preventing any flow through the contact interface. However, the porous medium option is not available for the overset mesh model in Ansys Version 2022 R2 or older versions that are used for this simulation. Therefore, a thin layer of water existed between the geobag and the bottom of the channel.

#### **e) Material properties**

The fluid used in the present study is liquid water with a dynamic viscosity of 0.001003 kg/(m s) and a density of 998 kg/m<sup>3</sup>. The density, initial shape, filling ratio, mass, and thickness of the bags are according to Table 2.2. The gravitational acceleration is 9.81 m/s, and the atmospheric pressure is 101.325 kPa. It is worth mentioning that the density and volume for Table 2.2 are different compared with material properties of the experimental study of Table 2.1. This is because the geometry of the bags was created from the side-view photos of the bag, and the image of the bags was extruded

to create the geometry. As a result, the extruded image possesses a greater volume than the physical bag. To match the experiment’s mass, it’s necessary to reduce the density of this extruded geometry.

Table 2.2: Material properties of the simulated geobag

Name	Material	Initial shape	Fill ratio	Density (kg/m <sup>3</sup> )	Thickness (m)	Mass (kg)	Volume (m <sup>3</sup> )
C1	Cloth	Downstream	54	1289.39	0.014	0.234	0.000181
	Cloth	Even	54	1499.4232	0.014	0.234	0.000156
	Cloth	Upstream	54	1448.9	0.014	0.234	0.000161
C2	Cloth	Downstream	69	1320.2	0.015	0.299	0.000177
	Cloth	Even	69	1413.177	0.015	0.299	0.000212
	Cloth	Upstream	69	1471.836	0.015	0.299	0.000228
C3	Cloth	Downstream	84	1471.836	0.022	0.364	0.000247
	Cloth	Even	84	1445.878	0.022	0.364	0.000251
	Cloth	Upstream	84	1434.595	0.022	0.364	0.000253
G1	Geotextile	Downstream	54	1325.178	0.017	0.234	0.000176
	Geotextile	Even	54	1235.154	0.017	0.234	0.000189
	Geotextile	Upstream	54	1230.607	0.017	0.234	0.00019
G2	Geotextile	Downstream	69	1692.97	0.021	0.299	0.000176
	Geotextile	Even	69	1352.51	0.021	0.299	0.000221
	Geotextile	Upstream	69	1310.081	0.021	0.299	0.000228
G3	Geotextile	Downstream	84	1427.52	0.025	0.364	0.000254
	Geotextile	Even	84	1414.196	0.025	0.364	0.000257
	Geotextile	Upstream	84	1412.604	0.025	0.364	0.000257

## f) Near Wall Treatment

Near Wall Treatment (NWT) is a technique which is used in CFD simulations to model a turbulence flow near the wall. Due to the chaotic and unpredictable motion of fluid particles in turbulent flows, it is difficult to predict thoroughly how flow behaves near solid objects. The NWT technique is able to capture the viscous forces’ effects on the flow. The NWT divided the wall boundary layer into three different zones. The viscous sub-layer ( $y^+ < 5$ ) is a layer which is in direct contact with the solid wall. The flow behaviour of the fluid in this layer is dominated by its viscosity. This viscous sublayer is typically very thin, only a few micrometers thick, and proportional to the

molecular viscosity of the fluid. The next layer is the buffer layer ( $5 < y^+ < 30$ ), which is immediately above the viscous sublayer. In this region, the fluid is affected by both the viscosity of the fluid and the turbulent eddies in the outer region of the flow. The last layer is the log-law region ( $y^+ > 30$ ), which is the outermost region. In this region, the turbulence eddies are fully-developed and can be modeled with high Reynolds number turbulence models, such as the Reynolds-Averaged Navier-Stokes (RANS).

The  $y^+$  is a dimensionless parameter that represents the normalized distance of wall-adjacent nodes of mesh from the wall. The  $y^+$  is calculated from the following formula:

$$y^+ = \frac{\rho_w u_* y}{\mu_w} \quad (2.18)$$

In this equation,  $u_*$  is defined as friction velocity in the near wall region, and  $y$  is the distance from the wall. The friction velocity can be determined from the following formula:

$$u_* = \sqrt{\frac{\tau_{wall}}{\rho_w}} \quad (2.19)$$

Where  $\tau_{wall}$  is defined as the shear stress acting on the walls. The  $y^+$  value over the bag changes from 0.00004 to 24.9.

### 2.4.3 Verification and Validation

Validation process of the overset mesh technique encompasses a comparison between the velocity profile obtained from the computational fluid dynamics (CFD) model and the experimental data available from White [36].

The measurements taken in the experiment with a cement bag were used to validate the model. The cement bag employed in the experiment possesses dimensions of 18 cm in length and 14 cm in width, entirely filled with cement. The choice of a cement bag, rather than a geotextile or cloth bag, stems from the fact that the shape of the cement bag remained unchanged throughout the experiment, as it was filled solely

with concrete. In contrast, geotextile and cloth bags filled with sand experienced changes in shape over time. Hence, the velocity profiles of the cement bag were utilized for validation purposes instead of geotextile or cloth bags. The velocity profile was measured at five different locations: A-M, B-M, C-M, D-M, and E-M. Figure 2.9 shows the top view of the geobag and the location of the measured velocities.

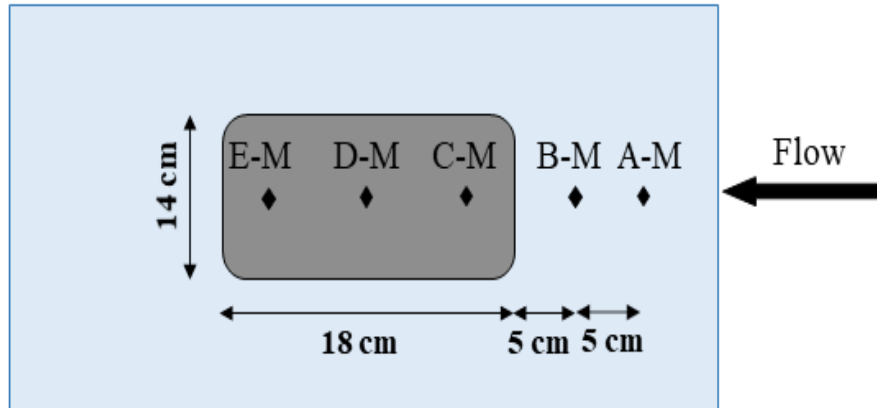


Figure 2.9: Locations of velocity profile measured upstream and on top of the cement bag

Figure 2.10 shows the velocity profiles of the cement bag at different locations. The average error for the A-M location, positioned before the bag, is determined to be 2.8%. Subsequently, the average errors for the B-M, C-M, D-M, and E-M locations are calculated as 3.4%, 4.2%, 6.8%, and 6.7%, respectively. Given that the errors across all plots are below 7%, it can be concluded that the overset mesh effectively represents the experimental data, which demonstrates the suitability of the overset mesh for accurately simulating the physical behaviour of the system.

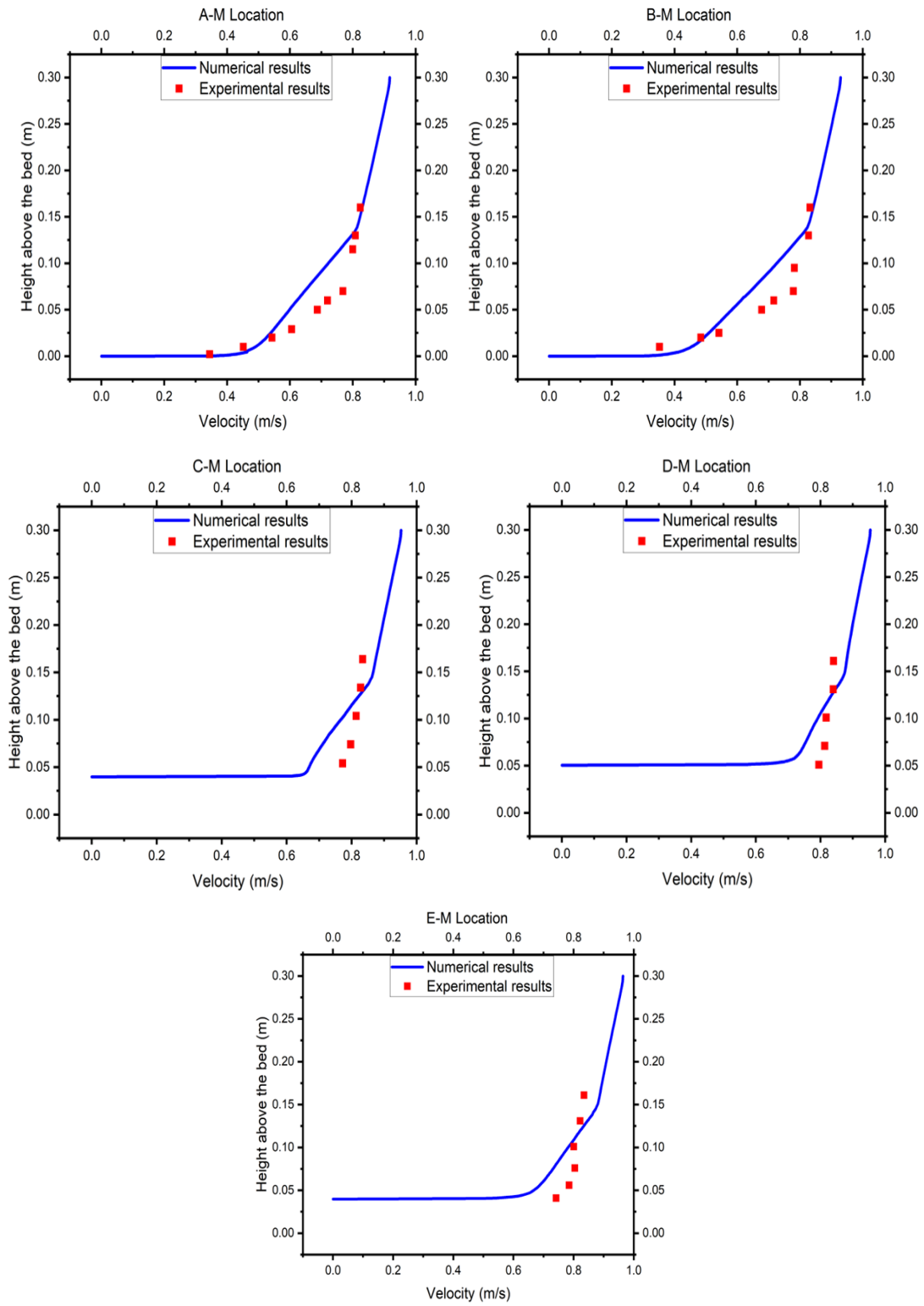


Figure 2.10: Comparing the velocity profiles of experimental data vs numerical simulation of the cement bag

## 2.5 Determining the effective-coefficient of geobag

The modeling of geobags positioned at the bottom of the channel presents certain limitations due to the presence of the thin layer of water between the bag and the bottom of the channel, which arises from the requirement of having a minimum of four layers of nodes between the bag and the domain wall in overset mesh modeling to prevent divergence. As a result, this thin layer negatively affects the precise net force determination in the vertical direction.

To address this issue, an effective coefficient was introduced into the simulation to compensate for the inherent shortcomings of the User Defined Function (UDF) in accurately incorporating the weight of the bag when calculating the summation of forces in the vertical direction. The effective coefficient was determined by dividing the drag force by its corresponding friction force at the time of maximum drag. The highest limit corresponds to failure velocity, and the lowest value corresponds to the maximum stable velocity of the geobag, and a range of effective coefficients was determined for each scenario. The intent was to create a correction that makes the resulting friction force equal to the drag force at the failure velocity. The effective coefficient was then multiplied by the friction force to simulate the movement of geobag at the failure velocity.

## 2.6 Determining Friction Coefficient

Laboratory experiments were conducted to determine the friction coefficient between the geobag and the flume bed. The friction coefficient is the tangent of the angle of friction, which represents the angle at which an object, in this case, the geobag, initiates sliding on an inclined surface. In the experiment, the geobag was carefully positioned on a ramp. The ramp was made of roofing asphalt (Manning's  $n = 0.0016$ ) since it represented the launched slope of geobags in the field. The angle of the ramp was gradually increased until the geobag began to slide. At this critical point, the

angle of the ramp was measured, providing the angle of friction. By taking the tangent of the angle of friction, the static coefficient of friction can be determined [48]. Geobags were tested in dry and wet conditions. In the dry condition tests, both the geobag and inclined surface were devoid of moisture, while in the wet conditions, the bag was placed in the box of water, and then the geobag was placed on the inclined wet surface. Each test was repeated three times, increasing the precision of the results. Figure 2.11 shows the geotextile and cloth bags placed on the inclined surface. This coefficient serves as a crucial parameter in assessing the interaction between the geobag and the fluid flow, aiding in the prediction and analysis of the geobag's motion and stability. Three different geobags, namely cloth, geotextile, and cement bags, were tested to measure the friction coefficient of the bags. The results of this section are presented in the next chapter.

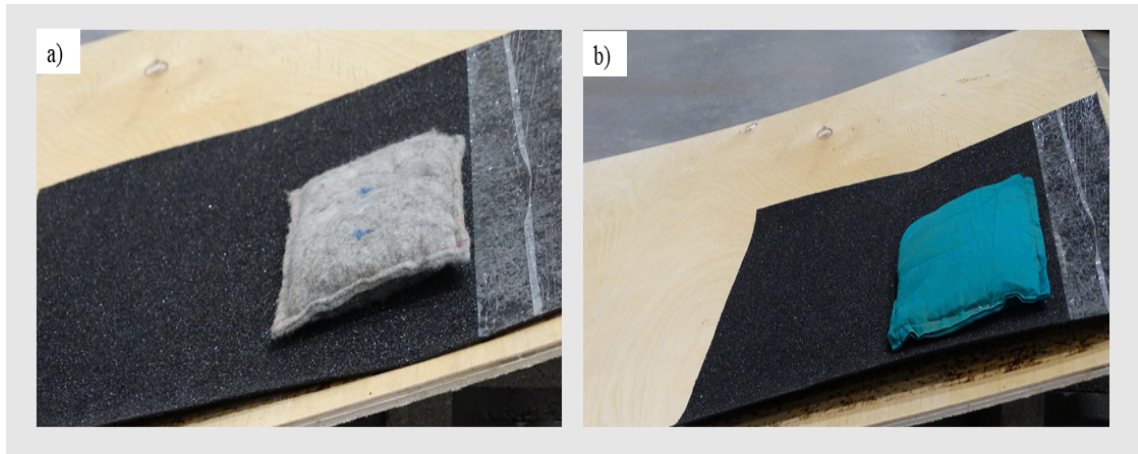


Figure 2.11: Geobag on the inclined surface

# Chapter 3

## Results and Discussion

### 3.1 Geometry of geobags prior to failure

The 18 scenarios investigated in the laboratory experiment [36] were considered in this study. For each scenario, the side view image taken just before failure was processed to generate the geometrical representation required in the CFD modeling. Figure 3.1 shows the geometry of all 18 scenarios. Each bag was arranged to have three different initial shapes, namely upstream heavy, downstream heavy, and even shape. The "Upstream heavy shape" denotes a configuration in which there is a greater concentration of sand towards the upstream end of the geobag. Conversely, the "Downstream heavy shape" signifies a configuration where there is a higher concentration of sand in the downstream section of the geobag. Lastly, the "Even shape" indicates a balanced distribution of sand throughout the geobag. For each bag, three filling ratios (54%, 69%, and 84%) were used.

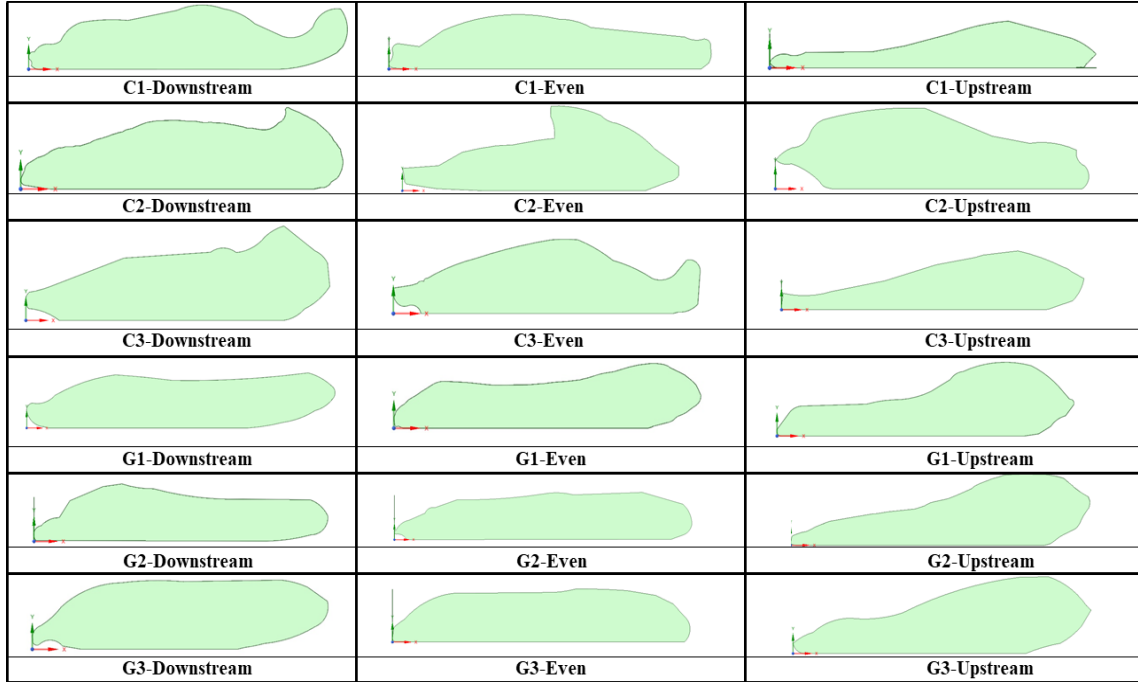


Figure 3.1: Geometry of cloth and geotextile bags used for modeling (C denotes cloth bag; G denotes geotextile bag; 1, 2, 3 indicates a fill ratio of 54%, 69%, and 84%, respectively)

## 3.2 The friction coefficient of bags

Table 3.1 summarizes the angle of friction for both dry and wet geobags determined in the laboratory test. It can be seen that the friction angle and friction coefficient of the cement bag placed on the wet surface are significantly lower than when placed on the dry surface. This is due to the lubricating effect of water on the inclined surface, facilitating the downward movement of the cement geobag at a smaller angle. However, this is not the case for the geotextile and cloth geobags. Water did not serve as a lubricant in these cases; instead, it adversely affected the friction behaviour at the interface, leading to an increase in the angle of friction and, subsequently, the friction coefficient between the bag and the wet surface.

A possible explanation is that the water content present in the wet geotextile and cloth geobags, initiated capillary forces between the sand grains. These capillary

forces induce cohesion among the sand grains and promote adhesion between the sand grains and the bag material. As a result, a stronger cohesion between the wet geobag and the inclined surface is established, ultimately leading to an increase in the friction angle for wet geobags. Thus, the presence of capillary pressure exerts a considerable influence, contributing to an amplified angle of friction. The capillary pressure causes uncertainty in the test for determining the friction coefficient. For this study, the dry coefficient is employed instead of the wet coefficient due to the unpredictable nature introduced by capillary pressure in wet conditions.

Table 3.1: The angle of friction and friction coefficient of geobag under dry and wet conditions

-	Material	Weight dry	Dry Angle	Friction coefficient	Average Friction coefficient	Wet Angle	Friction coefficient	Average Friction coefficient
1	Cement	1113.6g	28	0.53	0.49	15	0.26	0.24
			25	0.46		13	0.23	
			26	0.48		14	0.24	
2	Geotextile	375g	48	1.11	1.123	57	1.53	1.64
			48	1.11		59	1.66	
			49	1.15		60	1.73	
3	Geotextile	319.2g	46	1.03	1.03	60	1.73	1.68
			47	1		58	1.6	
			45	1.07		60	1.73	
4	Cloth	732.2g	43	0.93	0.943	49	1.15	1.11
			45	1		46	1.03	
			42	0.9		49	1.15	
5	Cloth	919.2g	43	0.93	0.965	48	1.11	1.03
			44	0.965		45	1	
			45	1		45	1	
6	Cloth	306.2g	46	1.03	1.06	48	1.11	1.083
			45	1		48	1.11	
			46	1.03		46	1.03	

### 3.3 The effective coefficient of bags

The range of the effective coefficient domain is provided in Table 3.2 for all geobags. By carefully examining the overlapping regions, the bags can be classified into five groups, as shown in Figures 3.2 and 3.3 for geotextile and cloth bags, respectively. It is evident that a significant degree of overlap exists among bags with comparable configurations. Notably, all downstream heavy shapes G1, G2, and G3 overlap at a specific range of effective coefficients and are therefore classified in Group B. Moreover, G1, G2, and G3, even shapes exhibit similar shapes before failure and overlap at a range of effective coefficients, placing them in Group C. However, no evident overlapping was observed for the upstream heavy geotextile bags, and they are categorized in Group A. This can be clarified by considering that the downstream portion of the bag moved upward prior to its failure, and the cross-sectional area for the drag force and, consequently, the drag force changed considerably before the failure.

The shape of cloth bags before failure is considerably different compared to their geotextile counterparts. Notably, all cloth bags with a downstream heavy initial shape displayed a similar shape just before failure which was denoted by a specific range of effective coefficients. Furthermore, C3-even, a specific downstream cloth bag, is characterized by a very similar shape observed in the other bags within this group, resulting in their classification under Group D. C3-even and C2 and C3-downstream shape did not experience failure in the experiment at the highest velocity setpoint of 1.08 m/s due to pump capacity limit[36]. Therefore, the upper bound of the effective coefficient could not be determined.

The remaining cloth bags did not display any similarity in terms of their shape. The range of effective coefficients also did not show any overlaps. This lack of overlap arises due to two potential factors: either the shape of the bags prior to failure is unattainable, or the bags experienced significant folding prior to failure, rendering accurate anticipation challenging.

Based on the bag shape and Table 3.2, a key observation is that the effective coefficient tends to decrease as the bag shape becomes more similar to that of an airfoil. The effective coefficient is the ratio of drag force to friction force obtained from Fluent, and the friction force is calculated by subtracting the lift from the weight force, which is then multiplied by the friction coefficient. A smaller value of the effective coefficient indicates that the model-calculated friction force needs to be corrected more due to a significant underestimation of the lift force. This was the case for the bags with more streamlined shapes (e.g. the geotextile bags with an even shape), the lift force is important for triggering failure, while CFD significantly underestimates the lift.

For the bags with a bulky and irregular front (e.g. G1-upstream, the cloth bags with a downstream heavy shape, C2-even, C3-even), the simulated lift force is closer to its physical value and thus needs less correction. This occurs because the simulated lift force is closer to its physical value, in comparison to the streamlined shapes. Consequently, the simulated friction force is less overestimated, resulting in a higher effective coefficient for bags with bulky shapes. As the values of the effective coefficient approach the unity, it means that less correction is needed.

To facilitate simulation and analysis interpretation within the same group, a single effective coefficient value was chosen for each group. Specifically, values of 0.27, 0.26, and 0.75 were assigned to Groups B, C, and D, respectively. Each of these values was selected based on being in the range of effective coefficient of all bags of the given group. Typically, these values are in the middle of the ranges to avoid margin values for friction force.

Table 3.2: Effective Coefficient domain for geobags

Name	Material	Initial shape	Fill ratio	Failure velocity	Maximum stable velocity	Effective Coefficient*
C1	Cloth	Downstream	54	0.75	0.71	0.63-0.76
	Cloth	Even	54	0.76	0.71	0.16-0.19
	Cloth	Upstream	54	0.79	0.76	0.23-0.29
C2	Cloth	Downstream	69	0.96	0.91	0.79-1
	Cloth	Even	69	0.86	0.81	0.2-0.75
	Cloth	Upstream	69	0.9	0.85	0.44-0.52
C3	Cloth	Downstream	84	1.01	0.96	0.71-1
	Cloth	Even	84	1.08	0.96	0.59-1
	Cloth	Upstream	84	0.97	0.87	0.33-0.43
G1	Geotextile	Downstream	54	0.51	0.49	0.12-0.28
	Geotextile	Even	54	0.63	0.61	0.147-0.28
	Geotextile	Upstream	54	0.75	0.71	0.875-1
G2	Geotextile	Downstream	69	0.61	0.55	0.24-0.28
	Geotextile	Even	69	0.74	0.72	0.26-0.28
	Geotextile	Upstream	69	0.81	0.77	0.399-0.411
G3	Geotextile	Downstream	84	0.78	0.74	0.21-0.26
	Geotextile	Even	84	0.78	0.76	0.24-0.26
	Geotextile	Upstream	84	0.94	0.92	0.245-0.263

Note: The higher value of the effective coefficient corresponds to the failure velocity and the lower value corresponds to the maximum stable velocity.

### 3.4 Effects of shape on the incipient motion of geobag

The bag with the same filling ratio but three different shapes was compared to assess the effect of shape on geobag stability. It is crucial to note that the shape of the bags modeled in this study represents their final shape just before failure. As a result, the bags may have experienced folding or significant changes in shape before reaching the failure point.

Figures 3.23, 3.5, and 3.6 depict pathlines of velocity magnitude for G1 downstream, G1 even, and G1 upstream shapes, respectively, at their corresponding failure

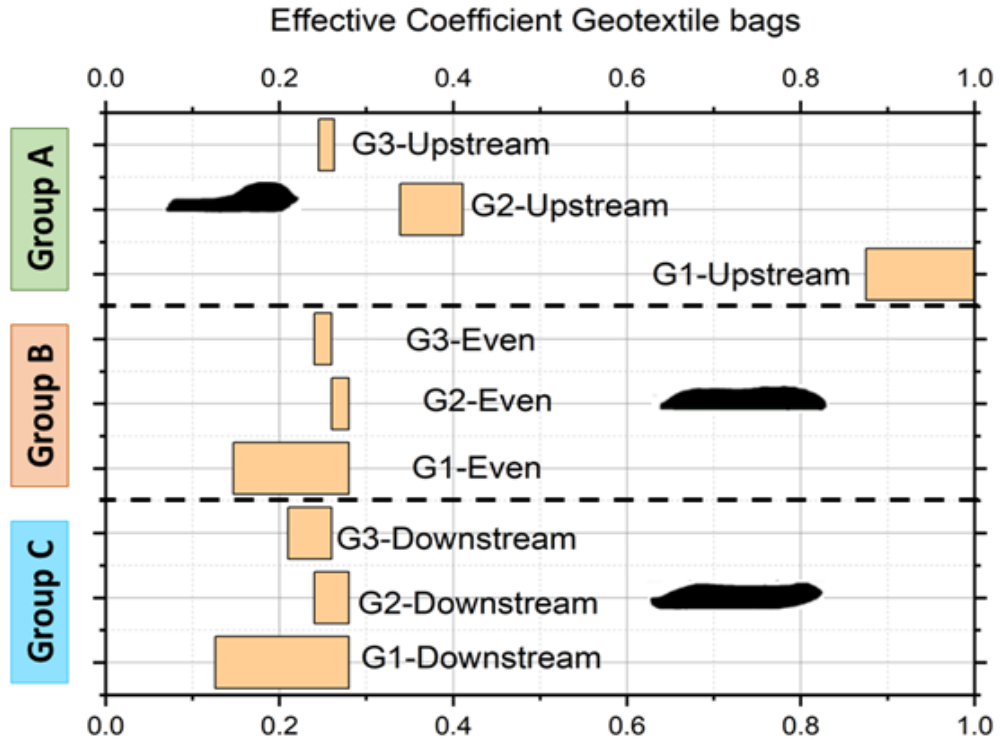


Figure 3.2: Effective coefficient for Geotextile bags

velocities. The velocity changes from 0 to 0.62 m/s for the G1 downstream shape, whereas, for the even and upstream shapes, the maximum velocity reaches 0.76 and 0.9 m/s, respectively. No re-circulation zone is observed in any of these figures. However, the G1 upstream shape experiences higher turbulence due to the blunt shape of the geobag.

According to the parallel lab experiment [36], the downstream heavy bag failed at lower velocities, suggesting that this bag is less stable as compared to the other two shapes[36]. This could be explained based on the shape of the geobag. Since the geotextile fabric is less flexible, the shape of the bag did not change much from the initial shape and was less susceptible to folding. As a result, the lift force plays a key role in the failure of the geotextile bags, and geobag begins to lift in response to the incoming flow. Since the downstream heavy shape is lighter in the upstream front,

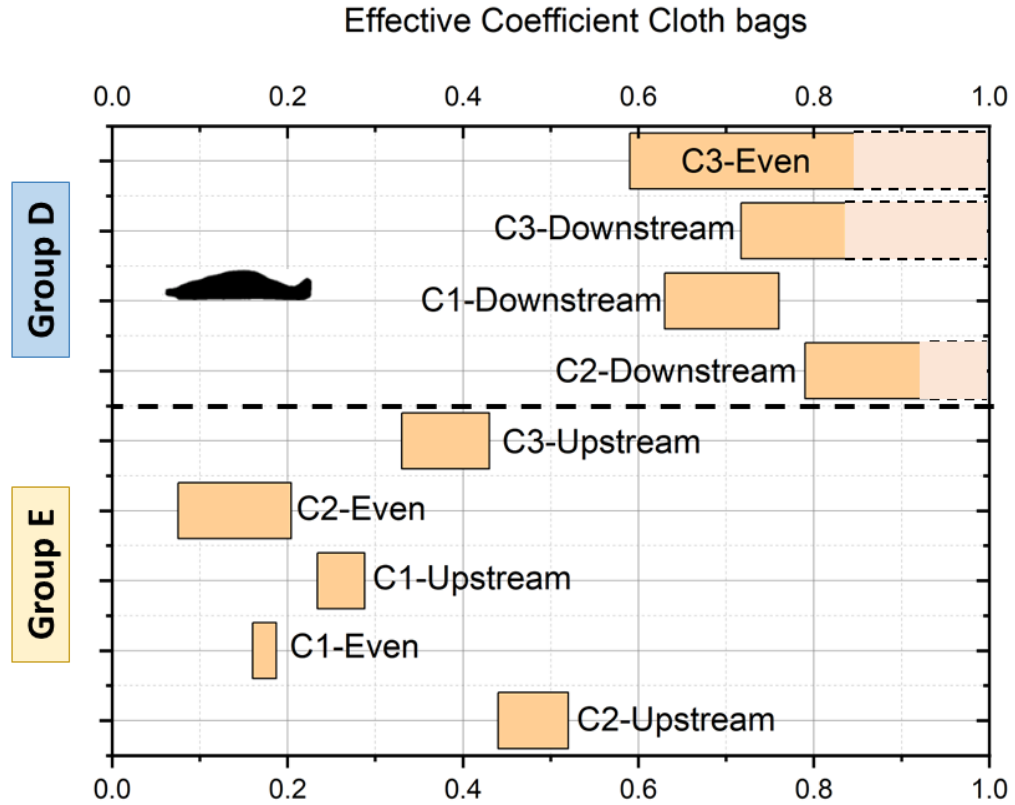


Figure 3.3: Effective coefficient for cloth bags

the bag is less stable, and lifting can happen sooner in response to upcoming flow.

On the other hand, the even and upstream-heavy shapes failed at higher velocities, implying a higher level of stability. This can be explained by the shape of the bags. The geobag is denser in the upstream region of the even and upstream shape bags, meaning that a higher amount of lift force is required to overcome the resisting force for the even and upstream heavy bags.

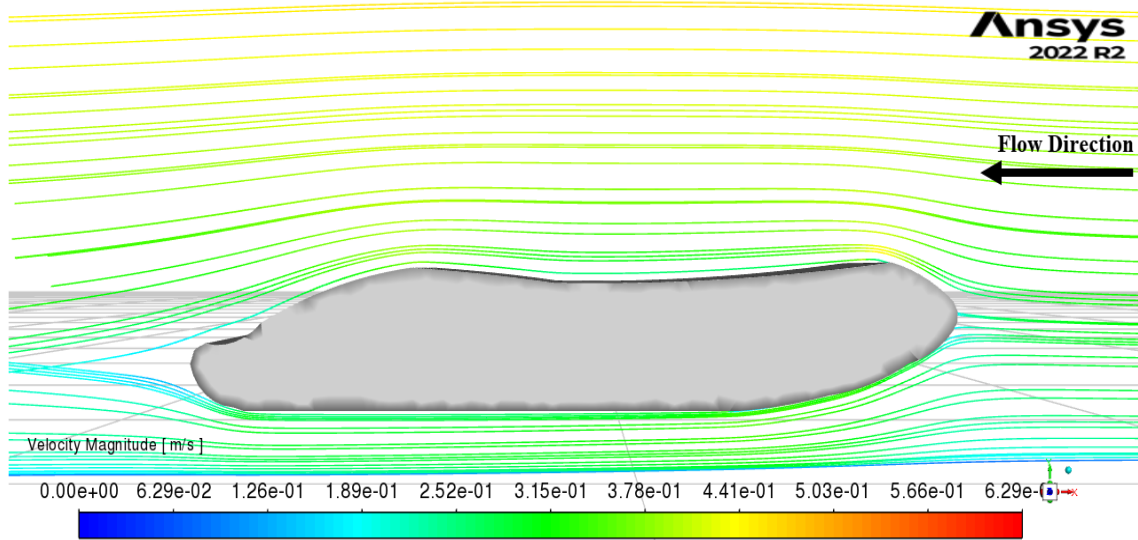


Figure 3.4: Pathlines of velocity magnitude at failure velocity 0.51 m/s for G1 downstream

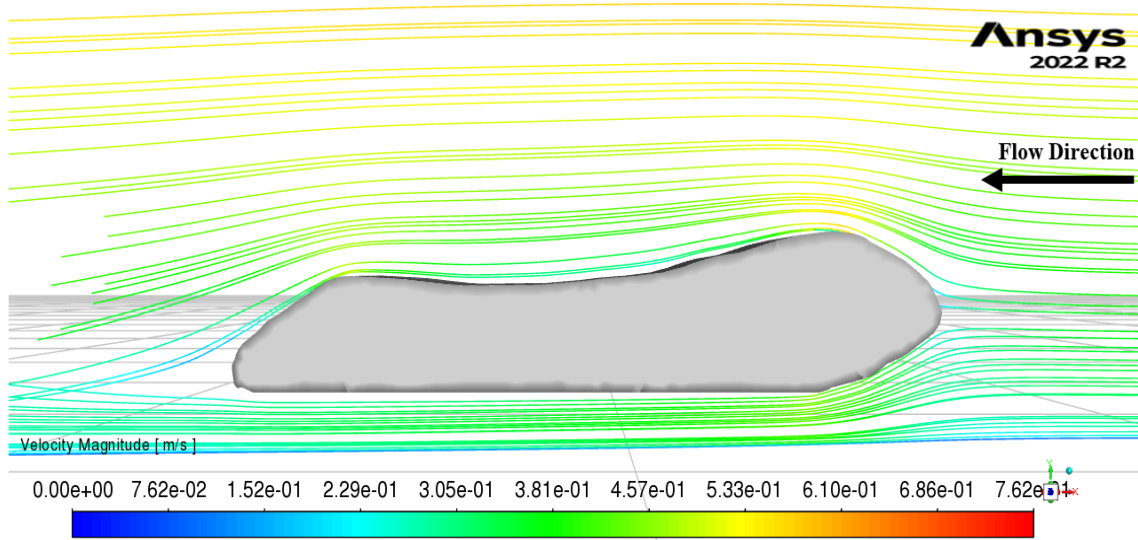


Figure 3.5: Pathlines of velocity magnitude at failure velocity 0.63 m/s for G1 even

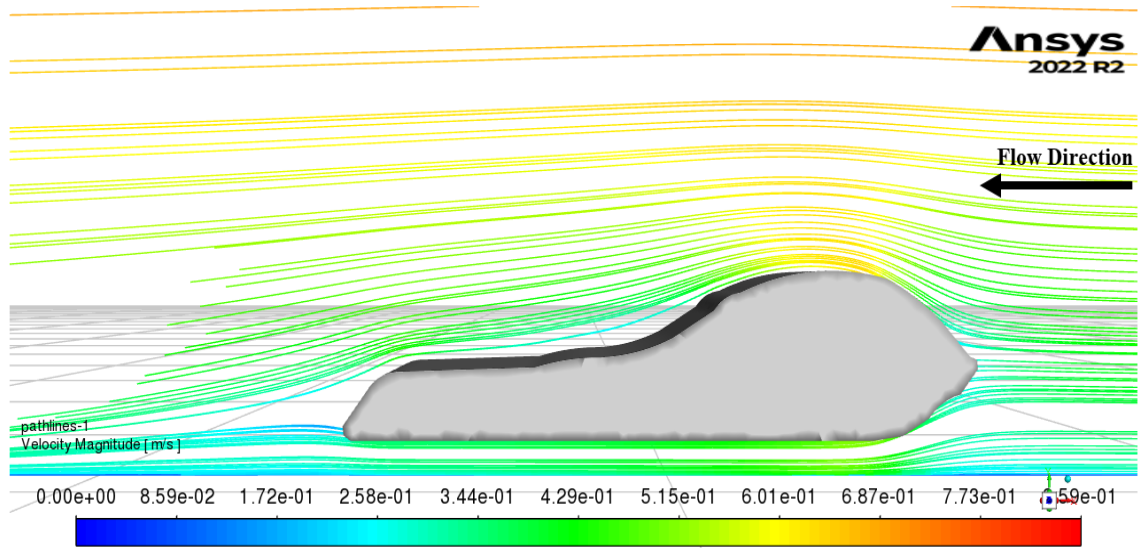


Figure 3.6: Pathlines of velocity magnitude at failure velocity 0.75 m/s for G1 upstream

Figures 3.7, 3.8, and 3.9 present the contours of static and total pressure for the G1 downstream, G1 even, and G1 upstream shapes of the geobags, respectively. Notably, the upstream heavy bag experienced the highest values of static pressure. The upstream heavy shape is denser in the region facing the upcoming flow, and the blunt shape causes a re-circulation zone and an area of higher pressure on top of the bag. The area of higher pressure on top and lower pressure on the bottom of the bag decreased the lift force, and as a result, a higher drag force was required to overcome the friction force and move the bag. The contours of static and total pressure for downstream heavy shape show a lower pressure difference between the front and rear of the bag. This is because the bag is lighter in the region of the upcoming flow, and failure happens at lower velocities since a lower lift force is required to lift the front of the bag and start the incipient motion of the bag at a lower pressure drag value.

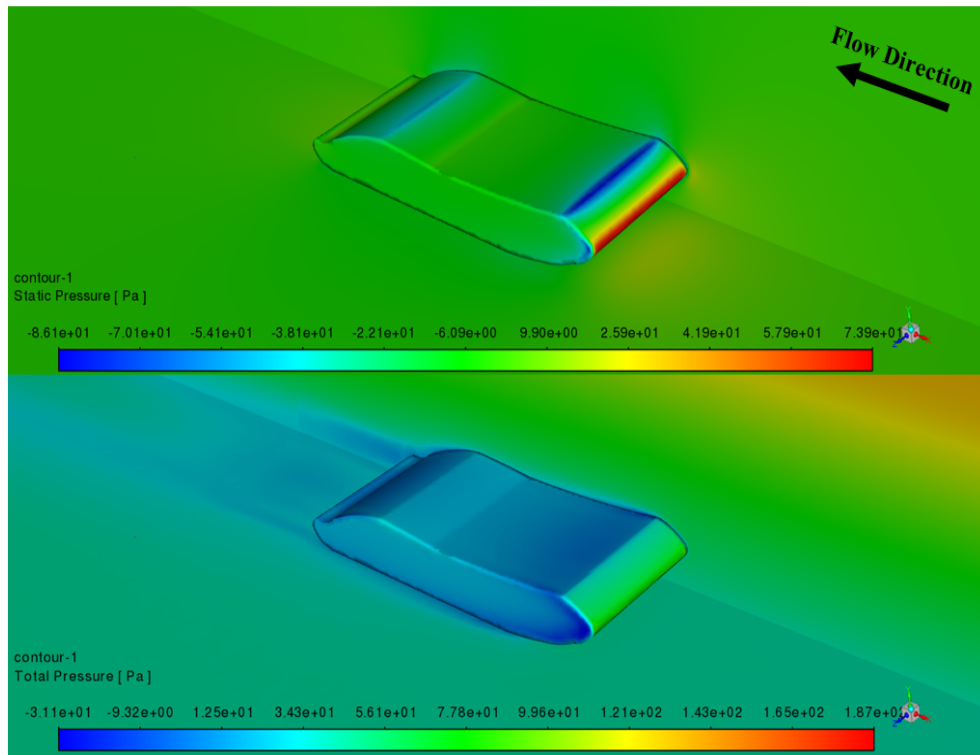


Figure 3.7: Contour of static and total pressure at failure velocity (0.51 m/s) for G1 downstream

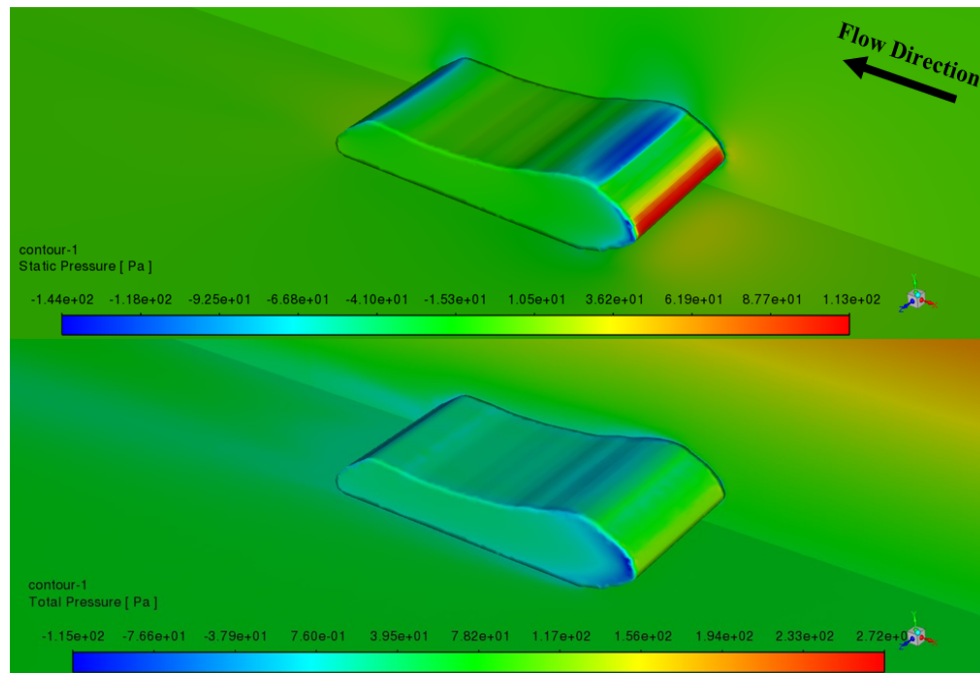


Figure 3.8: Contour of static and total pressure at failure velocity (0.63 m/s) for G1 even

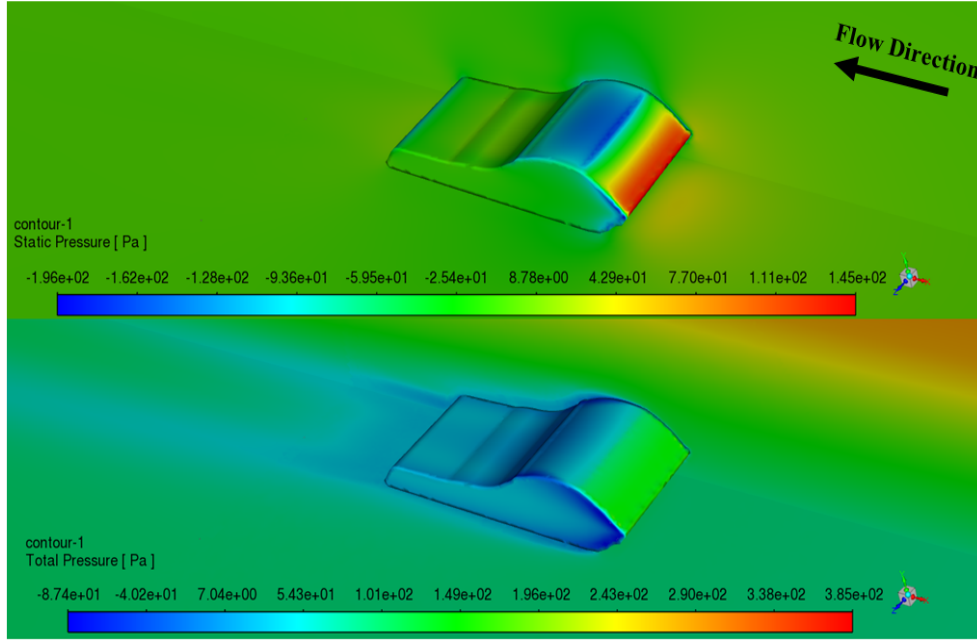


Figure 3.9: Contour of static and total pressure at failure velocity (0.75 m/s) for G1 upstream

Figure 3.10 compares the movement of geotextile bags during the simulation by examining the location of the center of mass versus time. In this Figure, the reference point is situated at the bottom-left corner of the geobag. Among the three bags of different shapes, the G1-even shape experienced the most significant displacement among the three bags. In contrast, G1 downstream and upstream shapes did not experience significant movement.

It is essential to mention that the rotational movement of the geobags was restricted in the simulation, limiting their motion to translational movement only. Consequently, there was no observed movement or motion in other directions, emphasizing the focus on translational displacement along the flow direction.

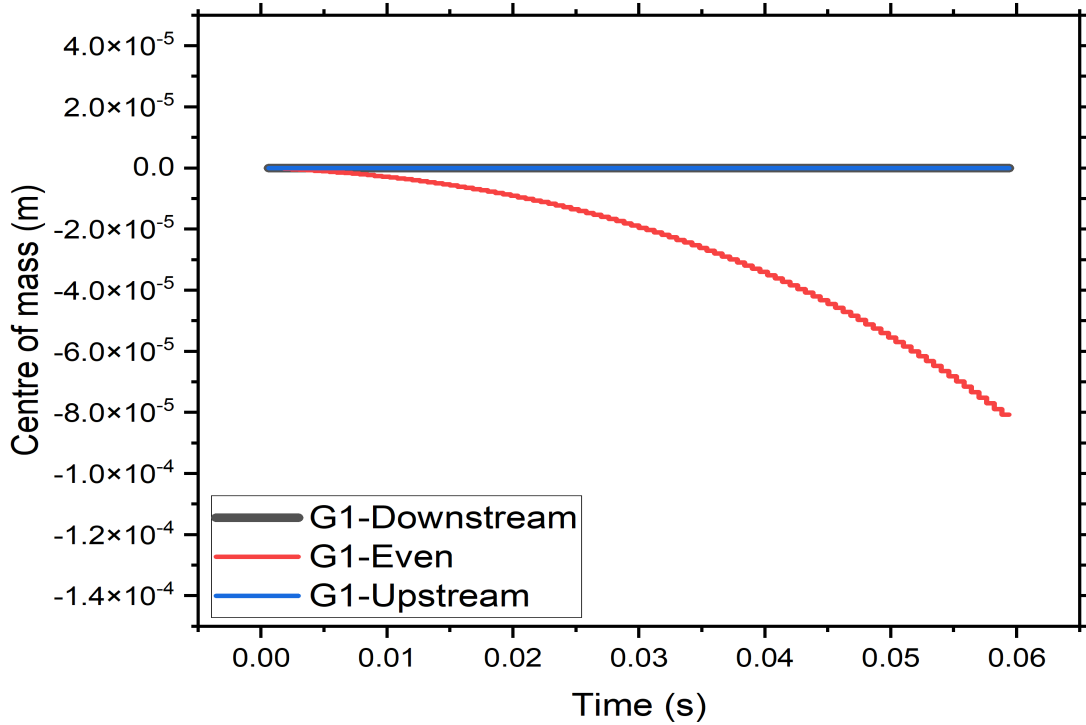


Figure 3.10: Plot of the center of mass at failure velocities for G1 downstream, even, and upstream with the effective coefficient (0.27 for G1 downstream, 0.26 for G1 even, 1 for G1 upstream )

Figures 3.11, 3.12 and 3.13 show the computed drag and friction forces versus time at their corresponding failure velocity for G1 downstream, G1 even, and G1 upstream shapes of the geobags. There is an initial change of drag and friction force before reaching a stable value. This abrupt variation arose from the occurrence of contact detection within the simulation during the initial time step. This phenomenon is due to the discretization process, and calculation error happens at the time of contact.

The geobags started to move when the drag force exceeded the friction force during the simulation. This happens at the velocity of 0.51 m/s for G1 downstream while the failure velocities are 0.63 m/s and 0.75 m/s for G1 even and G1 upstream, respectively. Although all cases have the same mass, G1-upstream experienced the smallest lift and the highest friction force among the three cases (Figure 3.13).

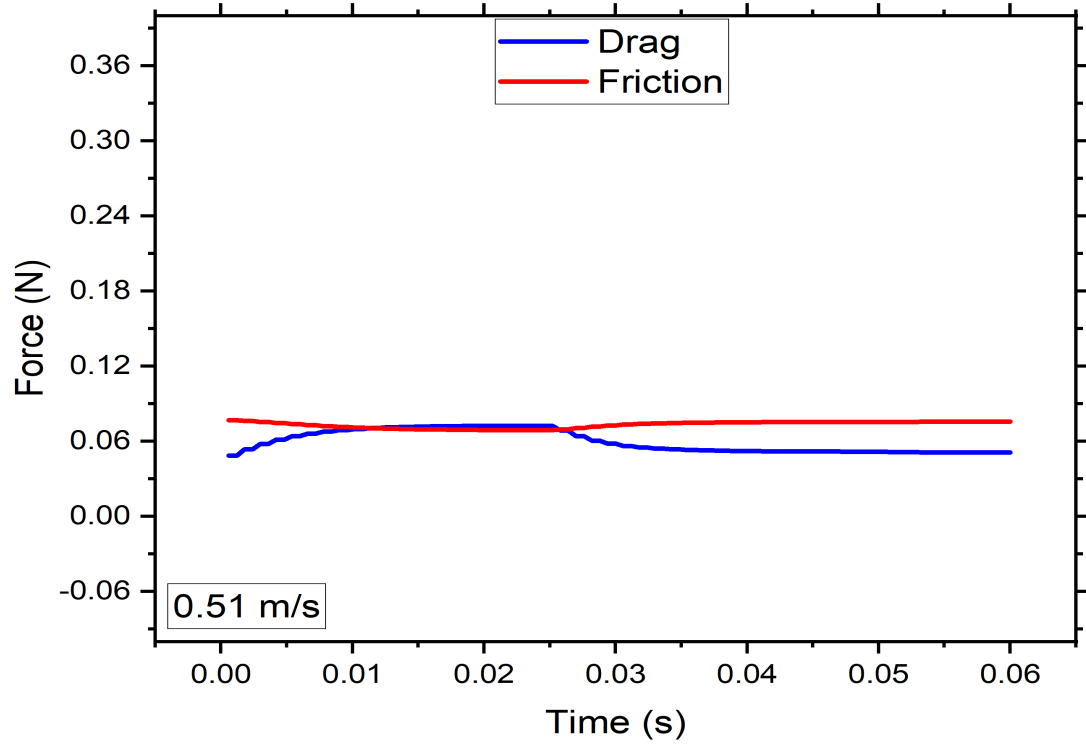


Figure 3.11: Drag and friction forces at failure velocity 0.51 m/s for G1 downstream with the effective coefficient (0.27)

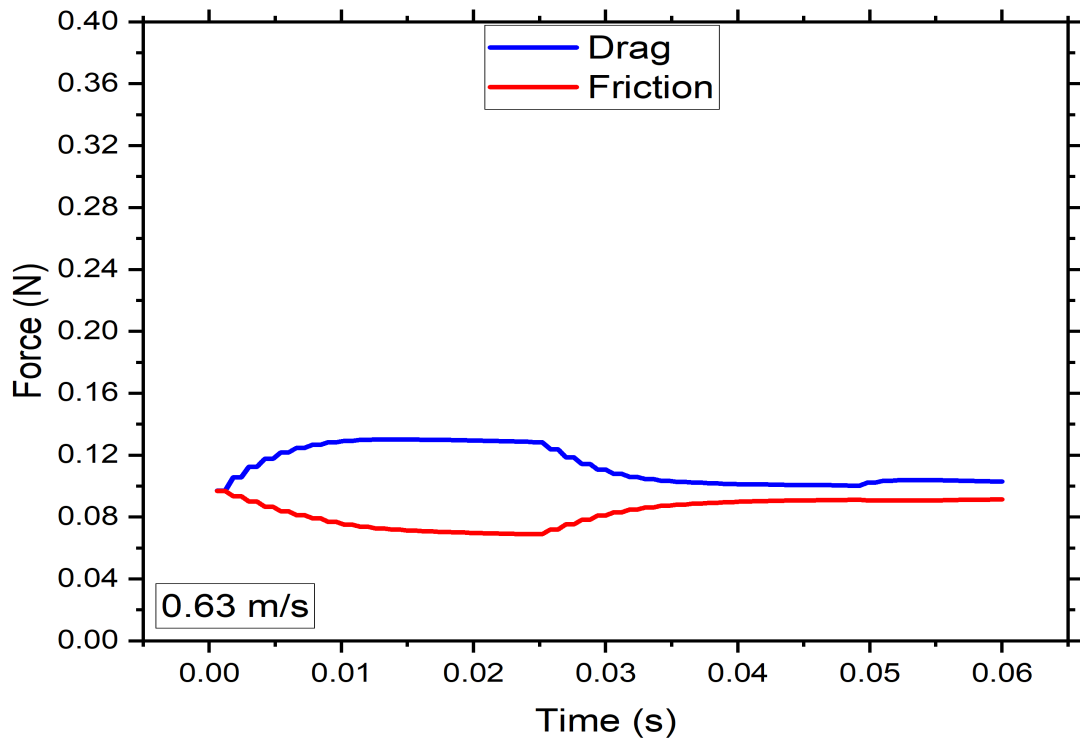


Figure 3.12: Drag and friction forces at failure velocity 0.63 m/s for G1 even with the effective coefficient (0.26)

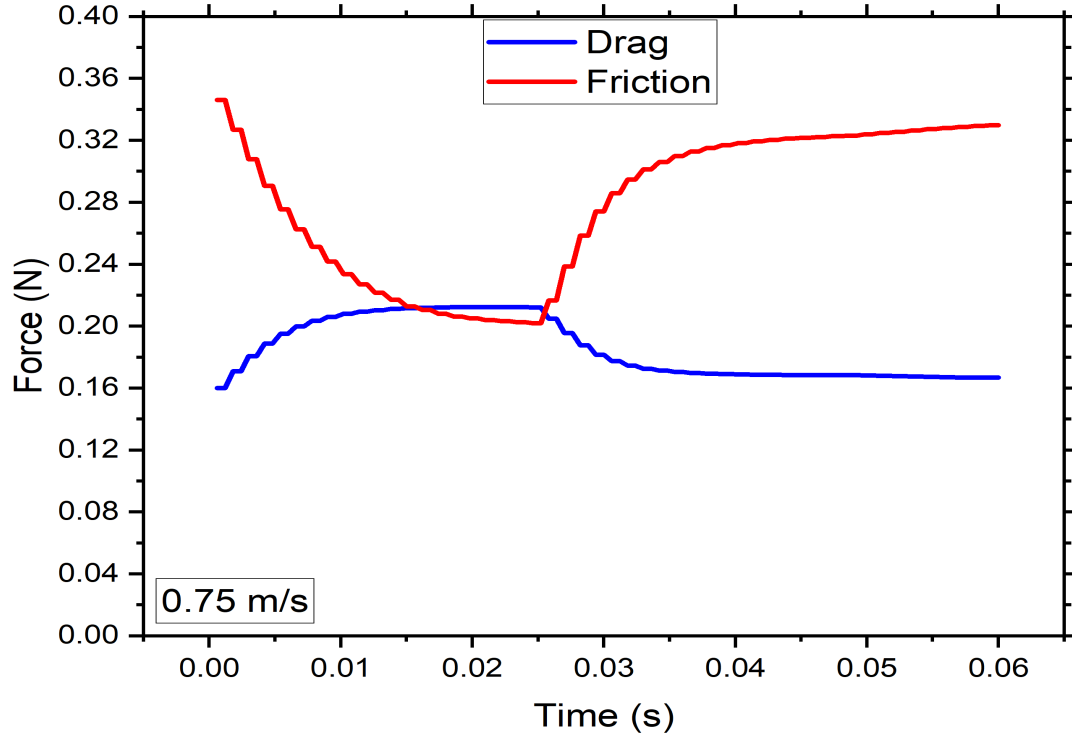


Figure 3.13: Drag and friction forces at failure velocity 0.75 m/s for G1 upstream with the effective coefficient (1)

### 3.5 Effects of material on the incipient motion of the geobag

This section compared the impact of the geobag material. To explore this aspect, two different geobags, each with the same filling ratio and shape but constructed from different materials, namely cloth, and geotextile, were compared. For this purpose, one representative geobag, which is the downstream shapes of both the cloth and geotextile bags, is examined to assess the material-dependent effects on the characteristics of the geobag. Different fabrics utilized in creating the geobags exhibit varying levels of flexibility. Increased flexibility leads to a greater propensity for geobags to fold and alter their shape prior to failure.

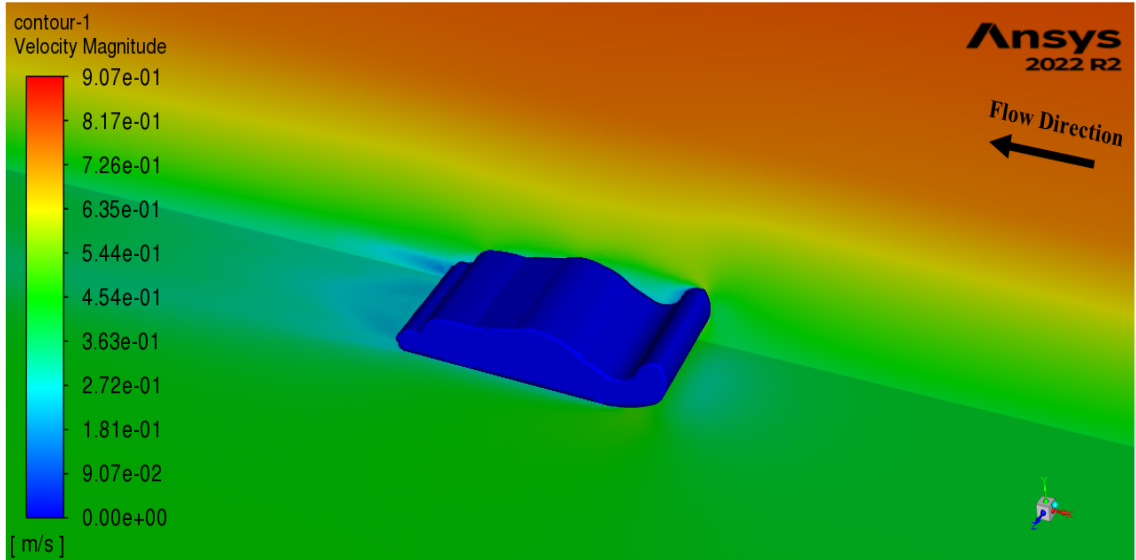


Figure 3.14: Contour of velocity magnitude at failure velocity (0.75 m/s) for C1 downstream

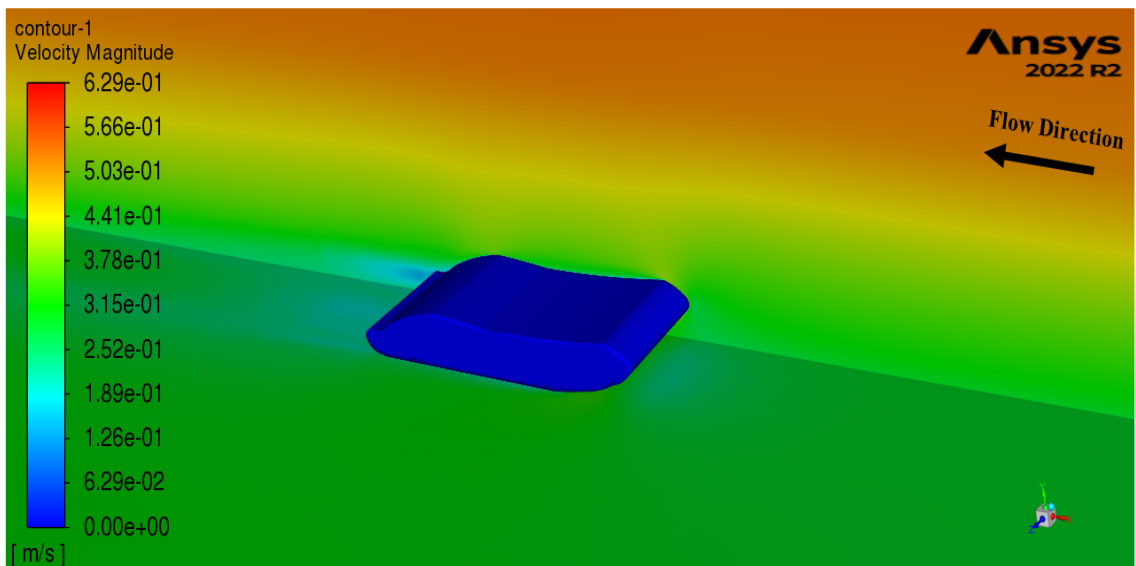


Figure 3.15: Contour of velocity magnitude at failure velocity (0.51 m/s) for G1 downstream

Figures 3.14 and 3.24 compared the velocity magnitude contours for two different downstream configurations, C1 downstream and G1 downstream, at their respective failure velocities. The failure velocities were 0.75 m/s for C1 downstream and 0.51 m/s for G1 downstream. Although the bags have the same weight and both of them have the downstream initial shape, the cloth bag has a higher failure velocity compared to

the geotextile bag. This is because the geotextile bags are less flexible and begin to lift from the approaching flow. This is not the case for cloth bags since cloth bags are either compressed or folded in on themselves due to higher flexibility. This explained the lift force for the failure of geotextile bags and the lower failure velocity for starting the incipient motion of geobag.

Figures 3.16 and 3.27 provide the contours of static and total pressure distribution for the C1 and G1 downstream geobags, respectively, at their respective failure velocities. Since the geotextile bag has less flexibility and is more streamlined in shape, the pressure of oncoming flow upstream of the bag causes lifting of the bag even at lower velocities. The incipient motion occurs at a lower velocity.

The pressure of upcoming flow folded the bag due to the higher flexibility of the cloth bag, This folding is clearly visible in the upstream section of the cloth bag. Therefore, the effect of the lift force is lower in a cloth bag and contributes to higher stability of the cloth bag.

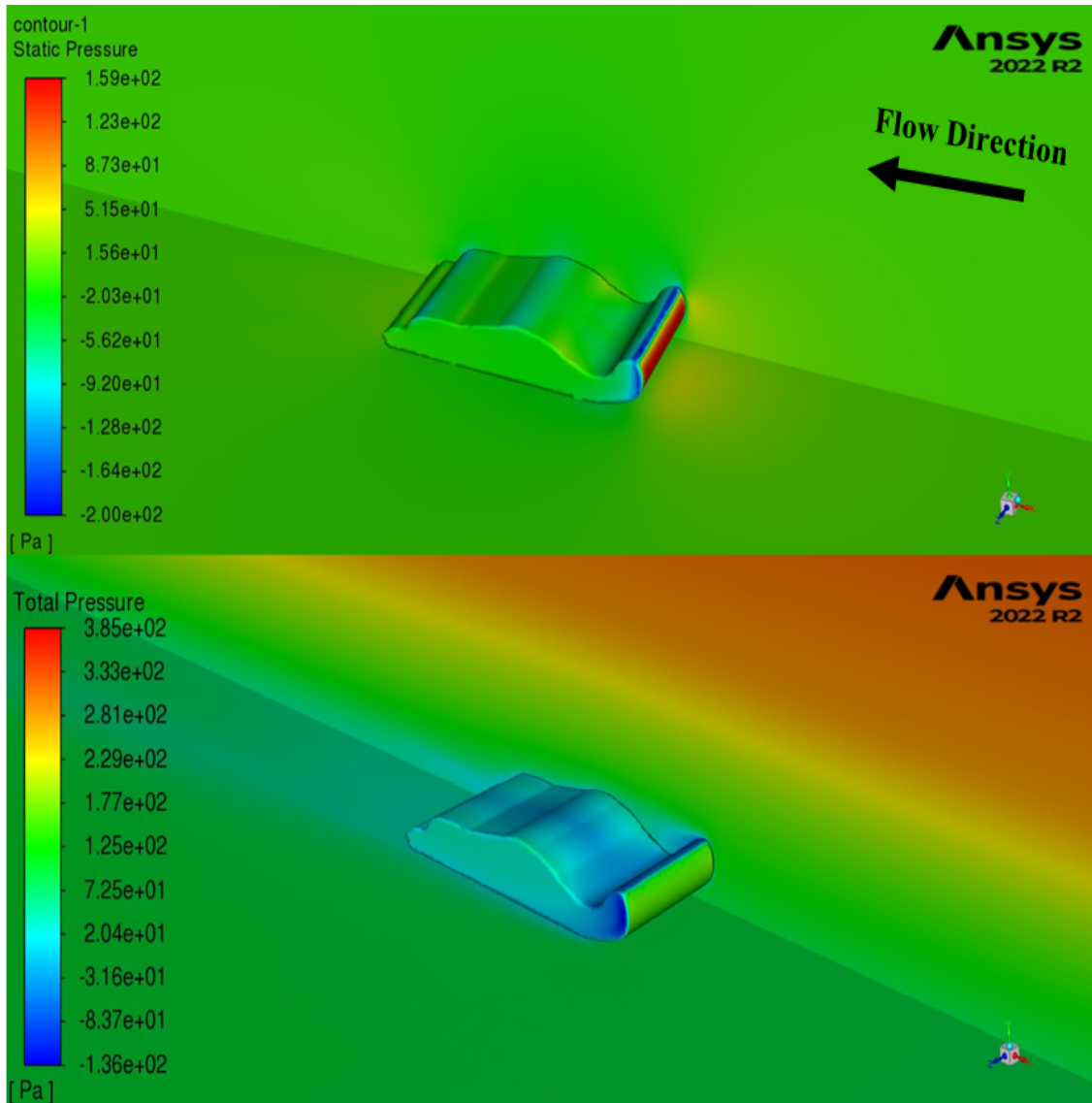


Figure 3.16: Contour of static and total pressure at failure velocity (0.75 m/s) for C1 downstream

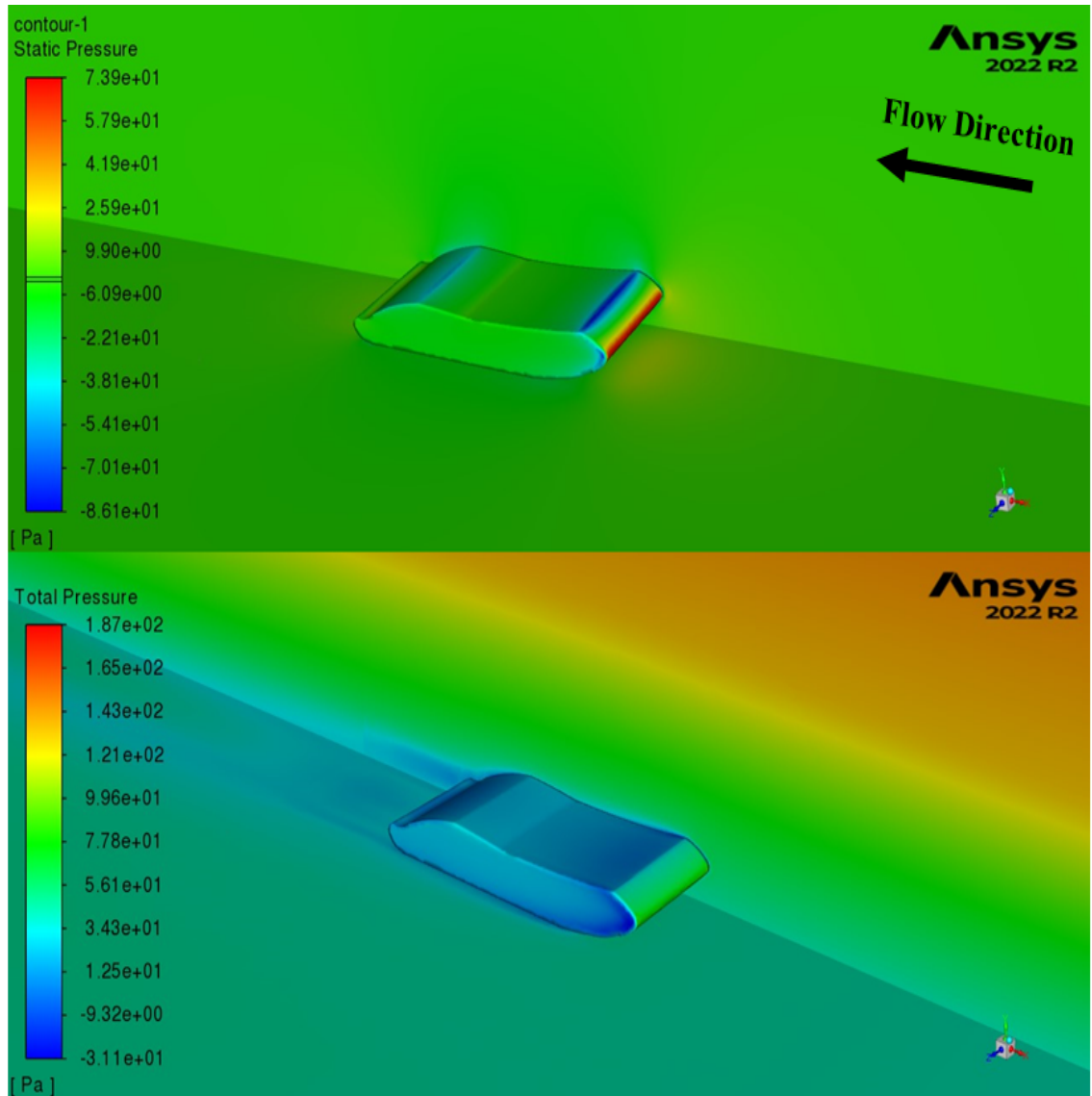


Figure 3.17: Contour of static and total pressure at failure velocity (0.51 m/s) for G1 downstream

Figure 3.18 shows the vector plot of velocity magnitude for the C1 downstream configuration at its respective failure velocity of 0.75 m/s. The vector plot shows the re-circulation zone on top of the cloth bag. As the fluid cannot follow the curvature of the bag surface and detaches from it, the flow separates from the surface and moves in the opposite direction, forming a re-circulation zone. The re-circulation zone occurred as a result of higher pressure differences around the bag, leading to a stronger adverse pressure gradient. The flexibility of the cloth bag makes it deform and adapt to changing flow conditions. In the presence of the re-circulation zone, the cloth bag experienced more significant and frequent deformations due to variations in flow velocity and direction, which caused the bag to be more stable and less affected by lift force. Similarly, Figure 3.19 displays the vector plot for the G1 downstream configuration at a failure velocity of 0.51 m/s. No re-circulation zone is observed in the G1 downstream shape, and less flexibility of the geotextile bag causes lifting of the bag in lower velocities, which makes it less stable compared with cloth bag.

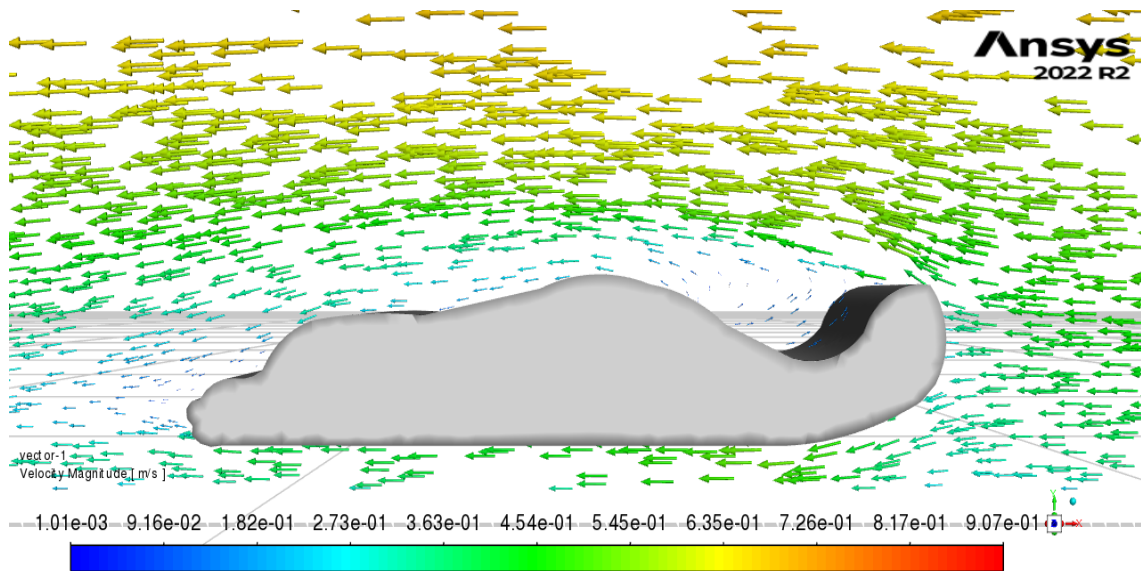


Figure 3.18: Vector plot of velocity magnitude at failure velocity of 0.75 m/s for C1 downstream

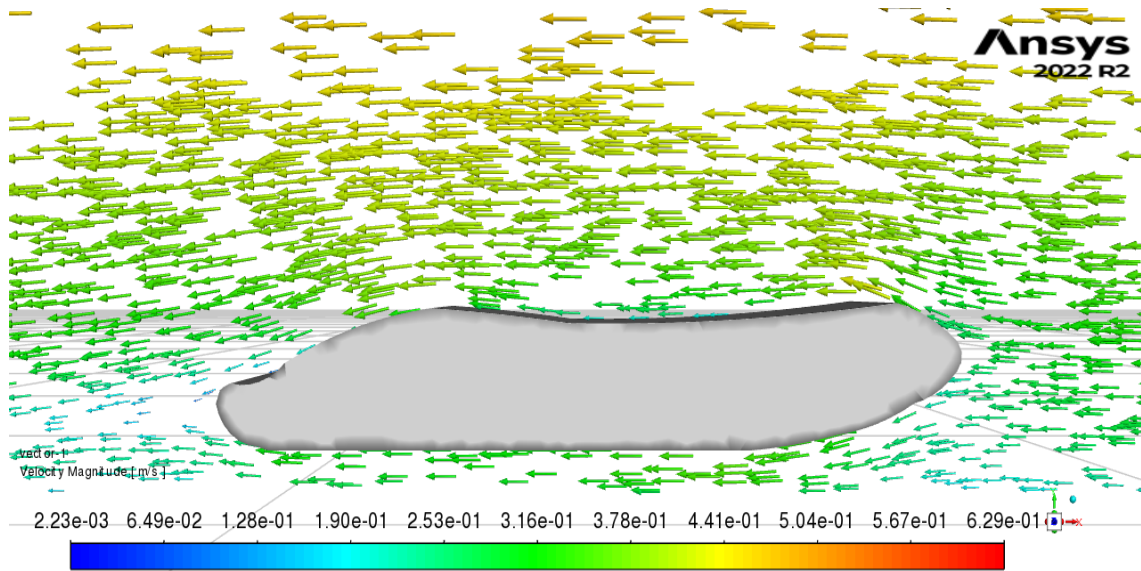


Figure 3.19: Vector plot of velocity magnitude at failure velocity of 0.51 m/s for G1 downstream

Figures 3.20 and 3.21 provide the plots of force versus time for drag and friction force in the modeling of geobag, offering a comprehensive understanding of the forces acting on the geobag during the simulation. Both C1 and G1 downstream shapes are plotted at the failure velocities of the geobag, signifying the critical point where the bags cannot sustain the flow conditions and experience failure. Even though both bags have the same weight, the drag force for the cloth bag is considerably higher than the geotextile bag. This can be related to the flexibility of the cloth bag since the C1 downstream shape experiences considerable changes in shape and fold before failure happens. A flexible geobag can deform due to fluid forces. The cloth bag remains stable at the higher velocity, which may be due to the upstream side of the cloth bag folding on top of itself. As a result, the cloth bag experiences less lift force and remains stable at higher velocities.

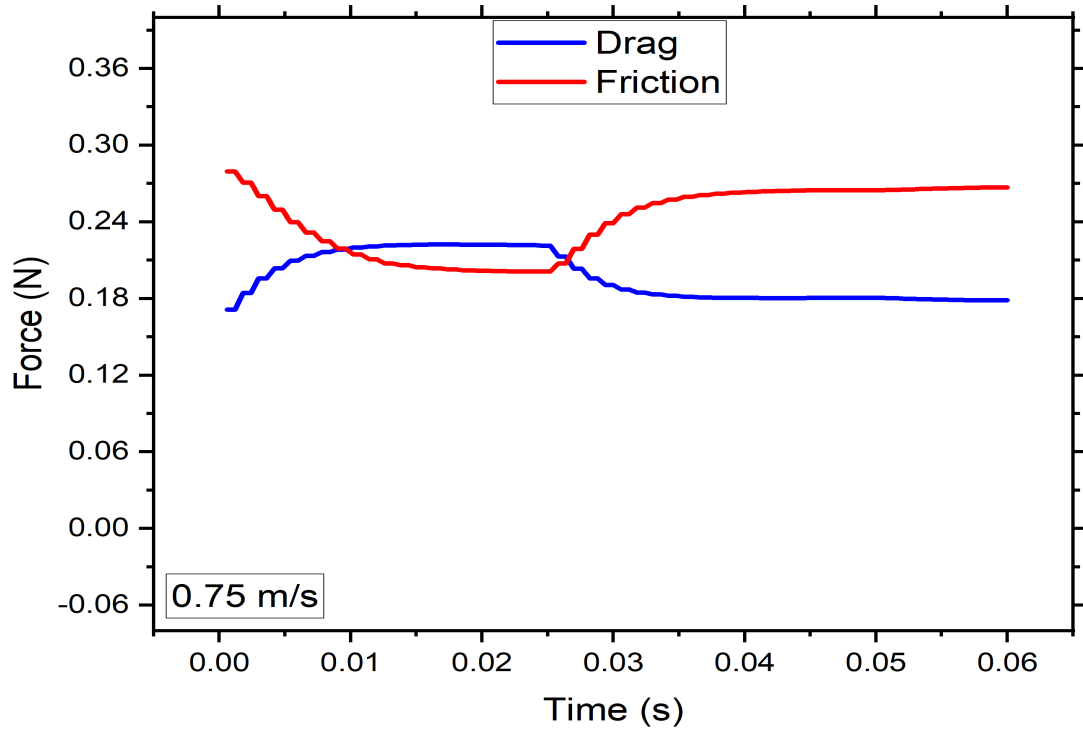


Figure 3.20: Plot of drag versus friction force at failure velocity 0.75 m/s for C1 downstream with the effective coefficient (0.75)

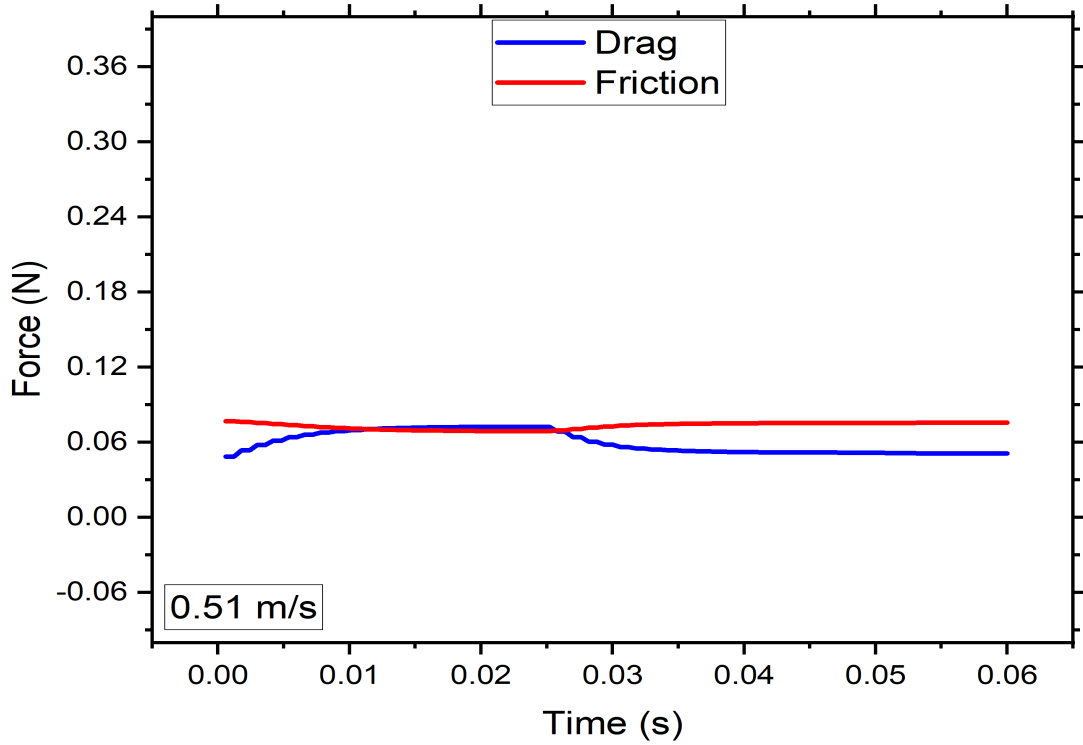


Figure 3.21: Plot of drag versus friction force at failure velocity 0.51 m/s for G1 downstream with the effective coefficient (0.27)

Figures 3.22 and 3.23 show the pathlines of velocity magnitude for C1 and G1 downstream shapes, respectively. Pathlines represent individual fluid particles as they move through the flow field. The pathlines reveal the separation and re-circulation on top of the cloth bag. The pathlines show where the fluid flow detaches from the surface of the cloth bag and forms re-circulation zones.

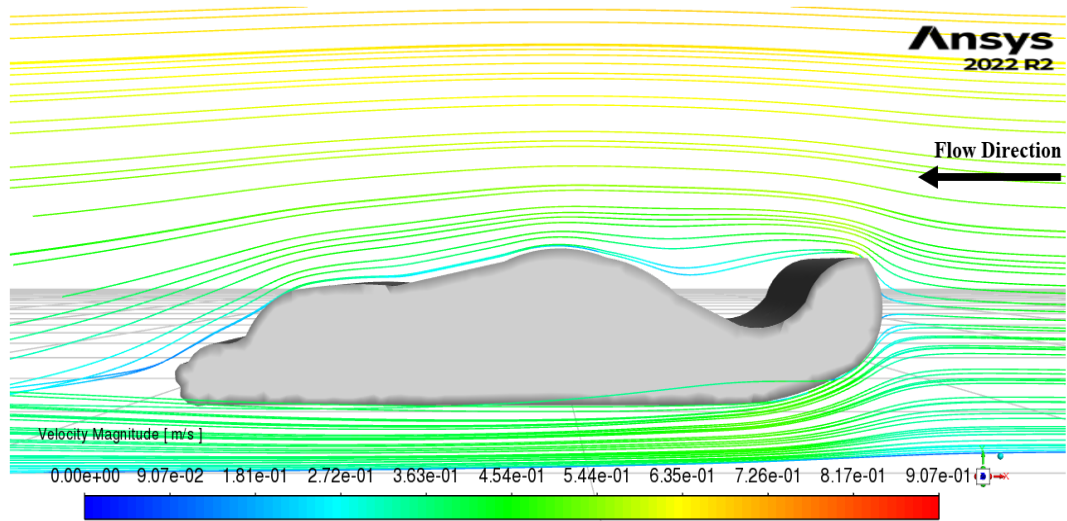


Figure 3.22: Pathlines of velocity magnitude at failure velocity 0.75 m/s for C1 downstream

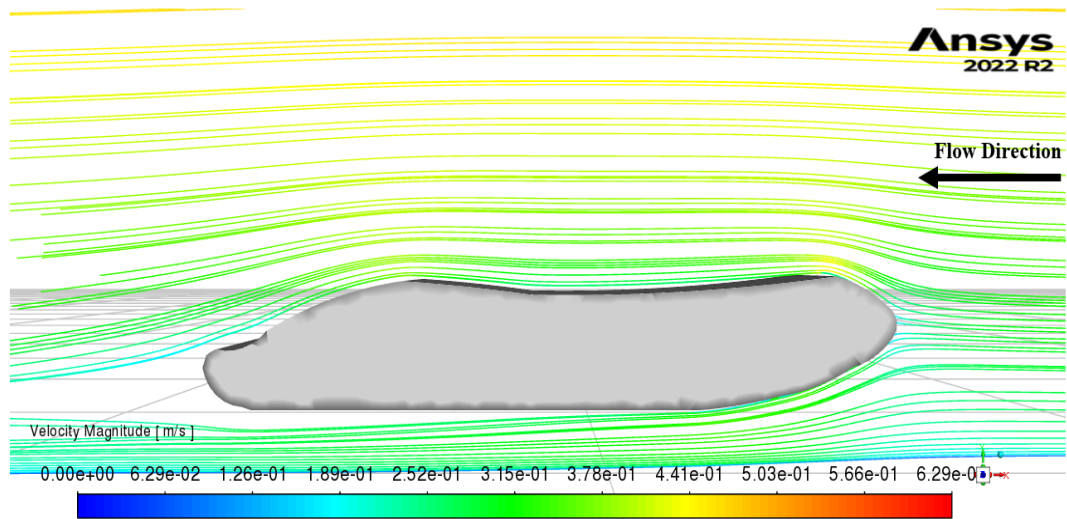


Figure 3.23: Pathlines of velocity magnitude at failure velocity 0.51 m/s for G1 downstream

In total, when evaluating the impact of material on geobag, it can be summarized as how much the material causes the flexibility of the geobag. As evidenced by the findings, cloth bags exhibit a higher degree of flexibility when compared to their geotextile counterparts. This heightened flexibility results in a substantial alteration of shape and folding of the bag on top of itself prior to failure. This causes a decrease in lift force for cloth bag. As a result, the cloth bags remain stable at higher velocities compared with geotextile bags.

### **3.6 Effects of filling ratio on the incipient motion of geobag**

This section focuses on exploring the effect of filling ratio variation on the behavior of geobag under turbulent flow conditions. By comparing three geotextile bags with different filling ratios while keeping other parameters constant, the aim is to investigate the weight of the bag on the incipient motion.

Figures 3.24,3.25 ,3.26 and provide a comparison of velocity magnitude contours for three different geobags: G1 downstream, G2 downstream, and G3 downstream, each with varying filling ratios of 54%, 69%, and 84%, respectively. Thompson et al, [35] show that bags with filling ratios of 80% are the most stable, and Pliarczyk et al,[26] indicated that a filling ratio of 80% prevents the sands from moving inside the bag. This means that bags with a higher filling ratio fail at higher velocities. The average failure velocities for G1 downstream, G2 downstream, and G3 downstream are measured at 0.51 m/s, 0.61 m/s, and 0.78 m/s, respectively [36]. This can be explained based on the weight of bags in the simulation.

Bags with a higher filling ratio experience higher gravitational and friction force require higher velocity and consequently, higher lift force to counteract this gravitational force and stay on the bottom of the channel. As a result, bags with a higher fill ratio require higher velocity to start the incipient motion.

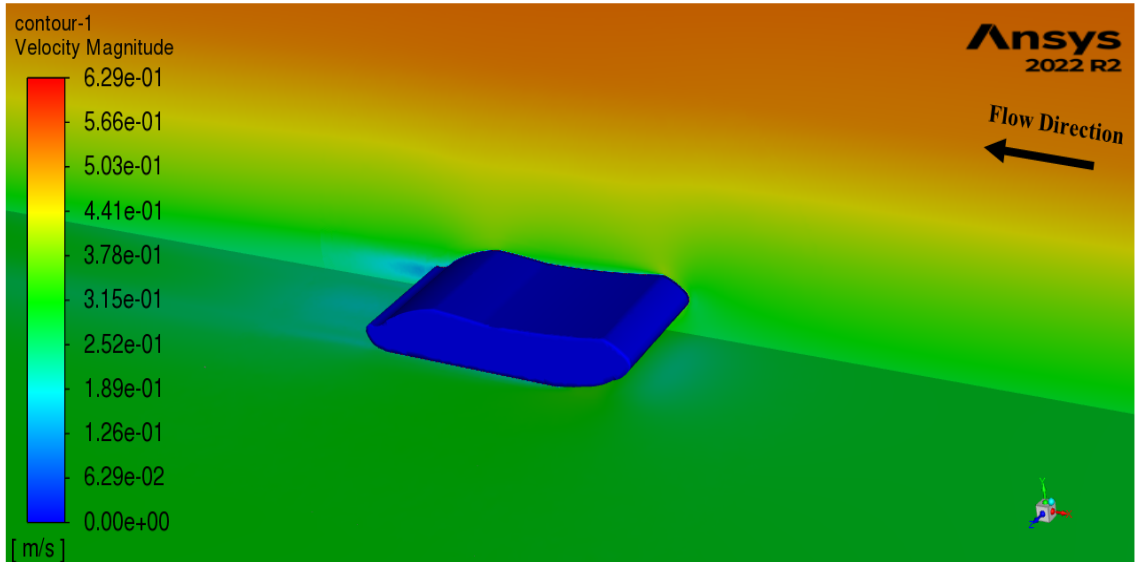


Figure 3.24: Contour of velocity magnitude at failure velocity (0.51 m/s) for G1 downstream

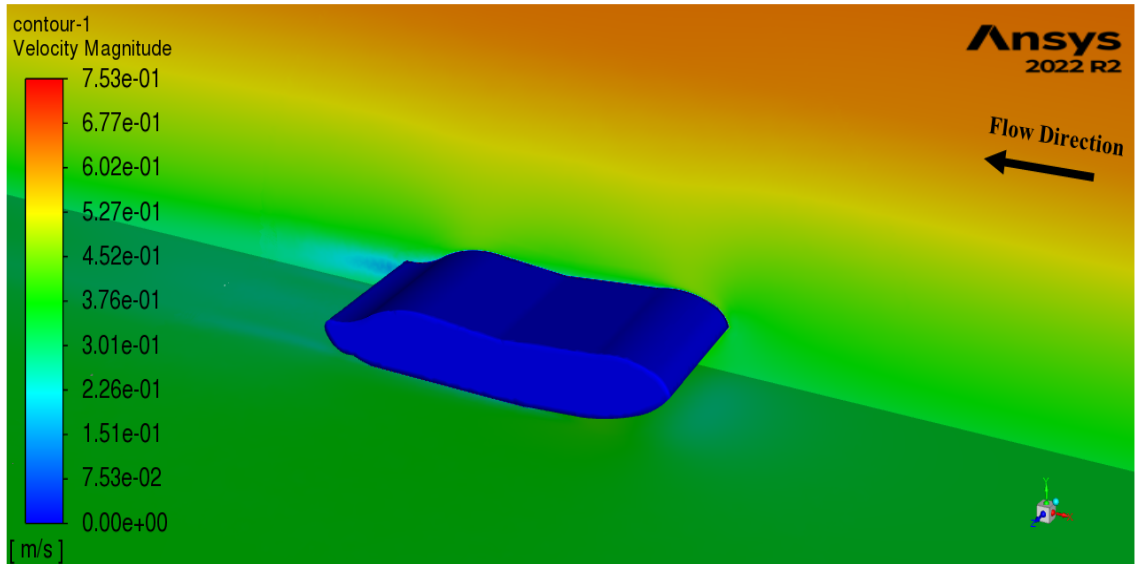


Figure 3.25: Contour of velocity magnitude at failure velocity (0.61 m/s) for G2 downstream

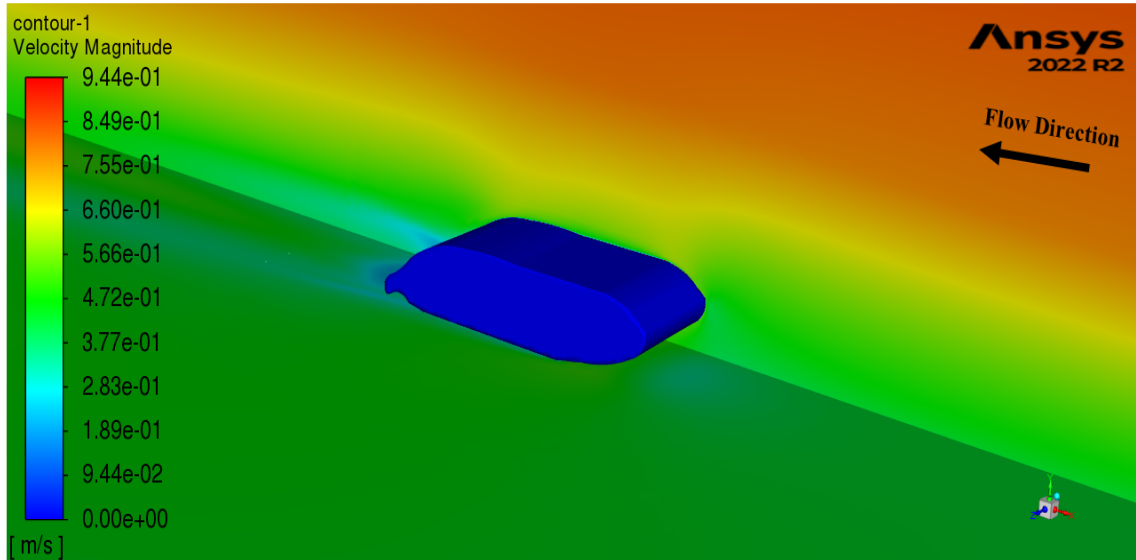


Figure 3.26: Contour of velocity magnitude at failure velocity (0.78 m/s) for G3 downstream

The contour of the total and static pressure for G1, G2, and G3 downstream geotextile bags is provided in Figures 3.27, 3.28, and 3.29. The highest static pressure is observed on the surface of the geobag facing the fluid flow, which is because the fluid flow comes to a complete stop at the surface of the geobag due to no-slip conditions. As the fluid flows across the upstream and moves towards the downstream of the geobag, the velocity increases and static pressure decreases. The pressure difference between these two regions causes pressure drag. In addition, the area with lower static pressure on top of the bag in the upstream region causes the bag to experience lift and makes the bag lighter, and decreases the friction force of the bag. This makes the bag move even with low drag force. This can explain why the G1 downstream shape has less stability and moves even with a lower drag force.

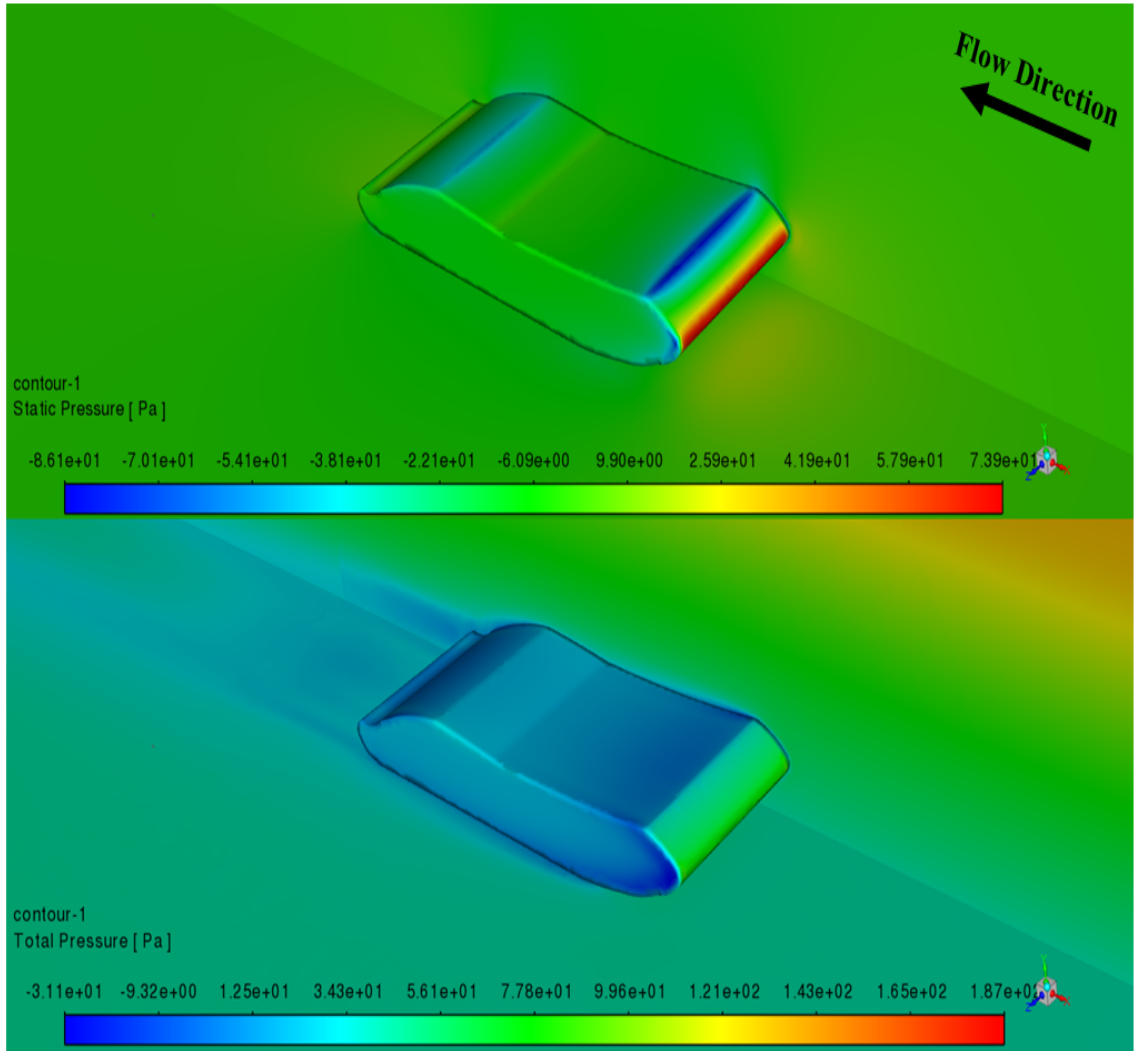


Figure 3.27: Contour of static and total pressure at failure velocity (0.51 m/s) for G1 downstream

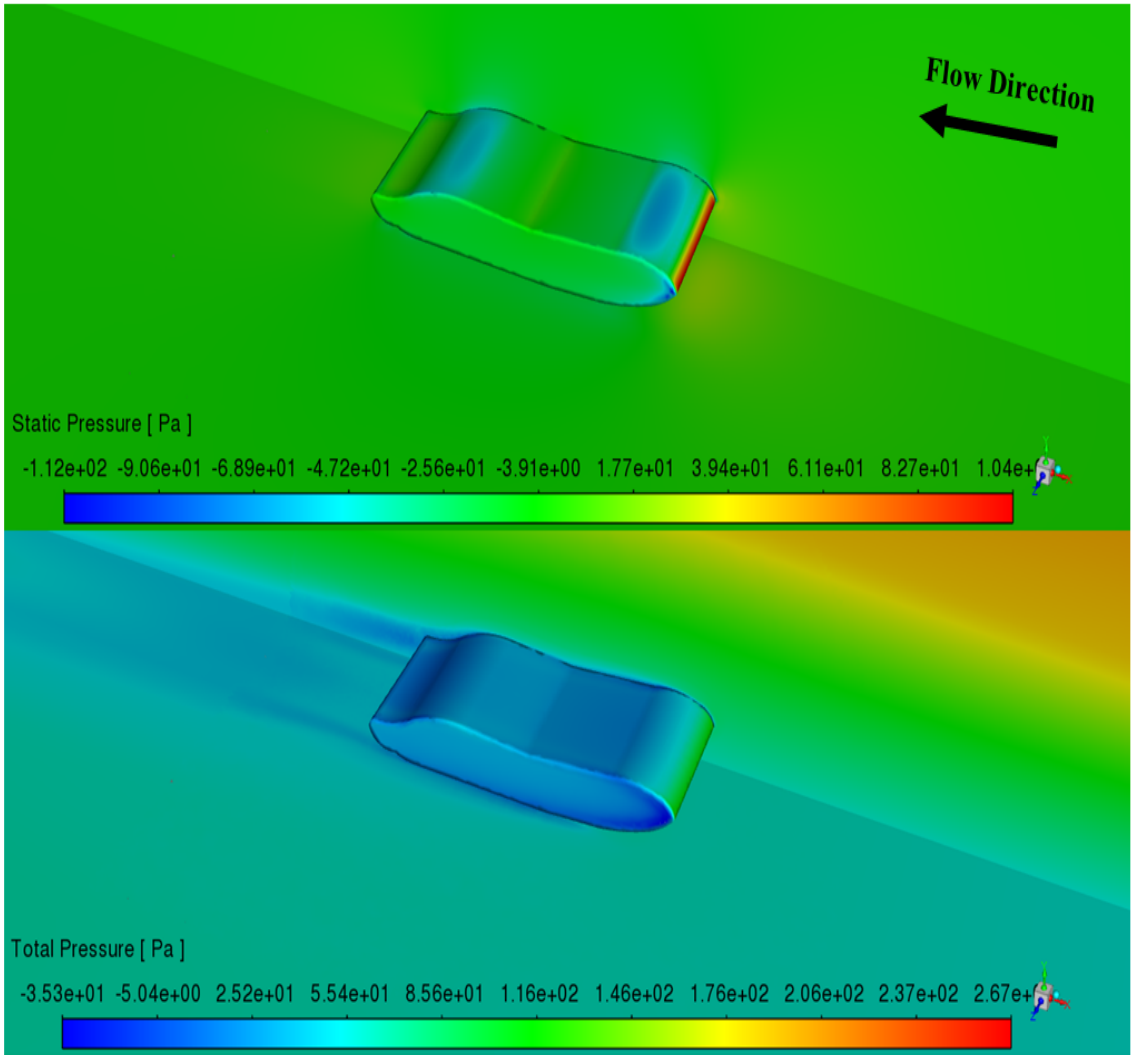


Figure 3.28: Contour of static and total pressure at failure velocity (0.61 m/s) for G2 downstream

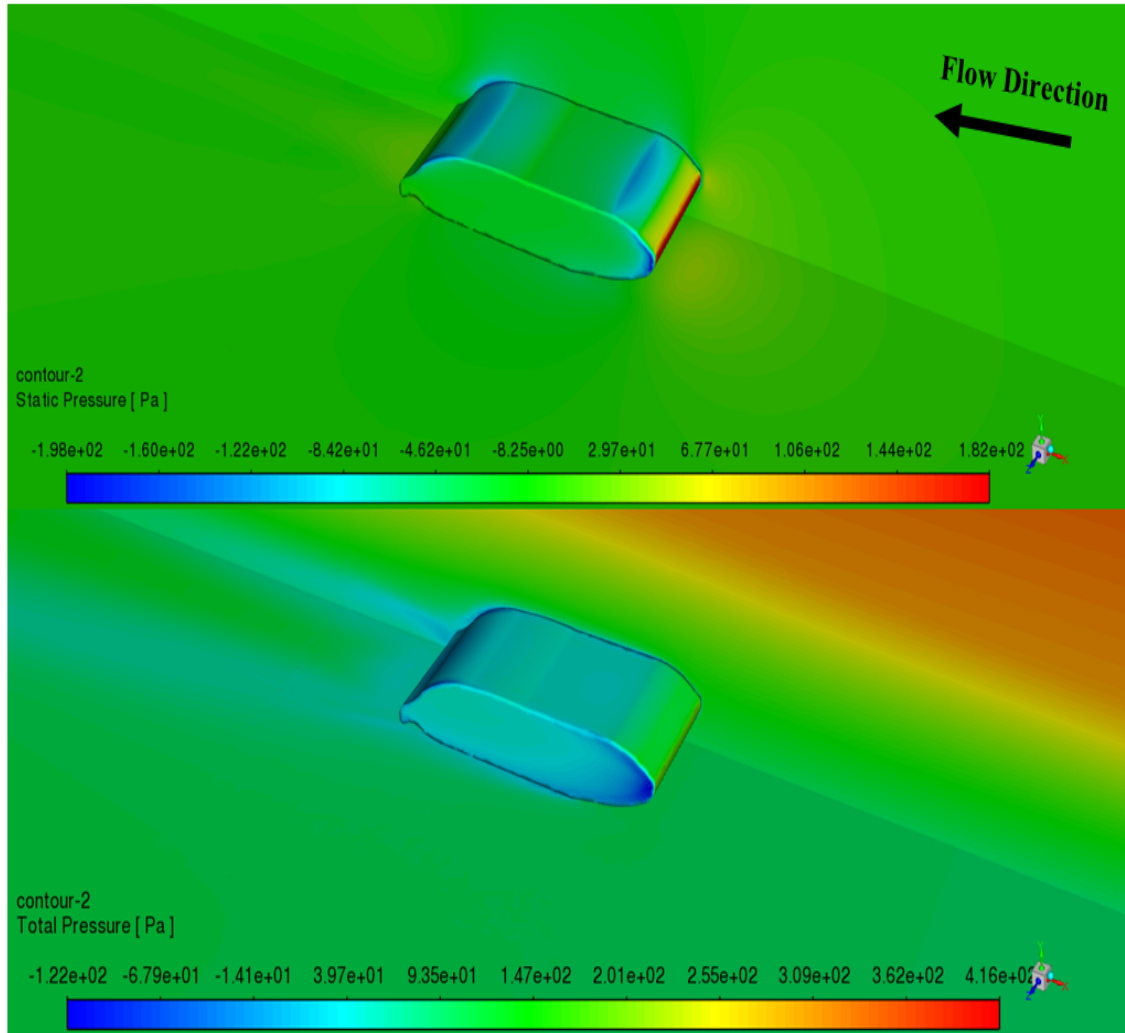


Figure 3.29: Contour of static and total pressure at failure velocity (0.78 m/s) for G3 downstream

Figures 3.30, 3.31, 3.32 and provide the plots of drag and friction forces versus time for the G1, G2, and G3 downstream shapes of geobags. All three figures are plotted at the failure velocity of the geobags, ensuring a consistent comparison under similar flow conditions. Drag force for G1 and G2 downstream at time steps of 0.01 to 0.03 seconds became more than the friction force and experienced the motion of geobag. For the G3 downstream, however, drag is more than the friction force at all timesteps, which shows considerable displacement for G3 downstream in the direction of the flow.

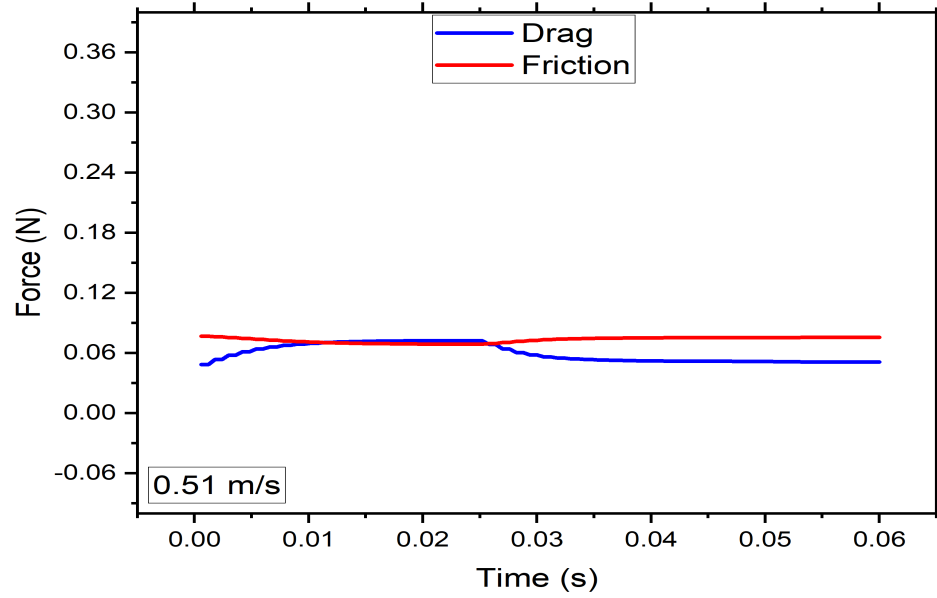


Figure 3.30: Plot of the drag versus friction force at failure velocity 0.51 m/s for G1 downstream with the effective coefficient (0.27)

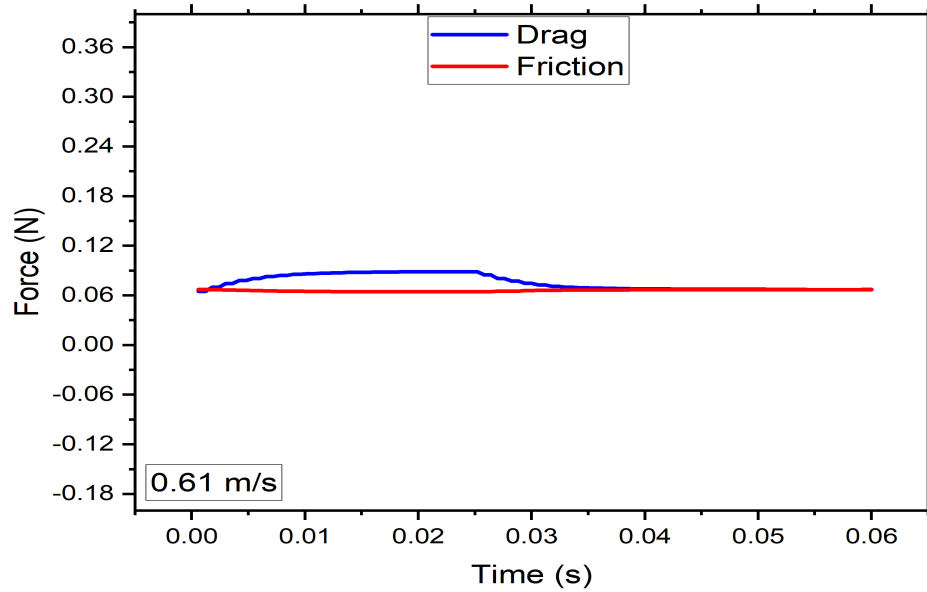


Figure 3.31: Plot of the drag versus friction force at failure velocity 0.61 m/s for G2 downstream with the effective coefficient (0.27)

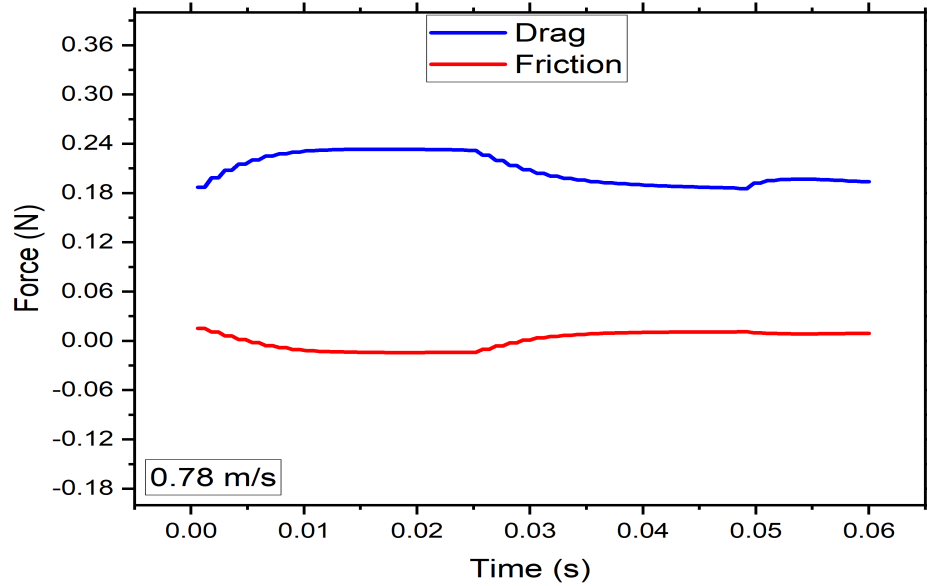


Figure 3.32: Plot of the drag versus friction force at failure velocity 0.78 m/s for G3 downstream with the effective coefficient (0.27)

### 3.7 The hypothetical geobag

Given the thorough comparisons conducted in the preceding sections, it becomes feasible that it is possible to compare any new shape of the geobag with groups of geobags presented in Figures 3.2 and 3.3 as long as they follow similar patterns. The objective of this section is to facilitate the comparison of any geobag with shapes resembling those presented in the mentioned figures, allowing for the determination of their failure velocities in the channel. For this purpose, one representative hypothetical geobag, which follows the shape of group B, is presented in this section. Table 3.3 shows the properties of the hypothetical geobag.

Table 3.3: Material properties of the hypothetical geobag

Material	Density (kg/m <sup>3</sup> )	Mass (kg)	Volume (m <sup>3</sup> )
Geotextile	1532.9	0.25	0.00016

It is worth mentioning that the effective coefficient for the hypothetical geobag is selected based on the effective coefficient of group B. Therefore, the effective coefficient 0.26, which is representative of group B, is selected for the hypothetical geobag as well.

Figure 3.33 shows the geometry of the hypothetical geobag. A detailed analysis of the hypothetical geobag is presented with various visualizations and plots at both the failure velocity and the maximum stable velocity. Contours of static and total pressure and plots of the center of mass and forces versus time are presented in this section. This approach allows us to investigate the effects of changing velocity on the behaviour of the hypothetical geobag.

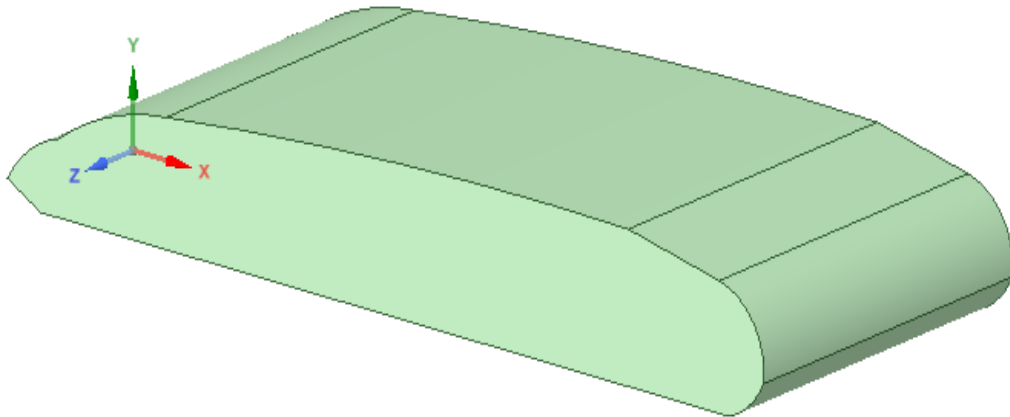


Figure 3.33: Geometry of the hypothetical geobag

The hypothetical geobag is simulated using an effective coefficient of 0.26, similar to group B, and the inlet velocity of the channel increased gradually by 0.05 m/s until the failure happened at a velocity of 0.95 m/s. Therefore, the plots and contours are presented at the velocity of 0.95 m/s and the maximum stable velocity, which is 0.9 m/s. Table 3.4 shows the average drag and friction force at maximum stable velocity and failure velocity of the hypothetical geobag.

Table 3.4: Average of Drag and Friction force affects the hypothetical geobag

Velocity (m/s)	Drag force (N)	Friction force (N)
Failure velocity (0.95 m/s)	0.157	0.19
Maximum stable velocity (0.9 m/s)	0.14	0.199

Figures 3.34 and 3.35 provide the contour of static and total pressure for the hypothetical geobag at the failure velocity of 0.95 m/s. The upstream of the geobag flow comes to a complete stop due to the presence of the geobag obstructing the flow. The fluid particles have to divert their path and flow around the geobag. This redirection of flow creates an area of low pressure on the upstream side of the body. On the downstream of geobag, the fluid particles re-converge after having flowed around the body. This re-convergence leads to a region of increased pressure compared to the upstream. The pressure difference between the upstream and downstream sides of the geobag contributes to a higher pressure drag force. This force acts in the direction opposite to the motion of the body and opposes its movement through the fluid, which in turn leads to resistance against the motion.

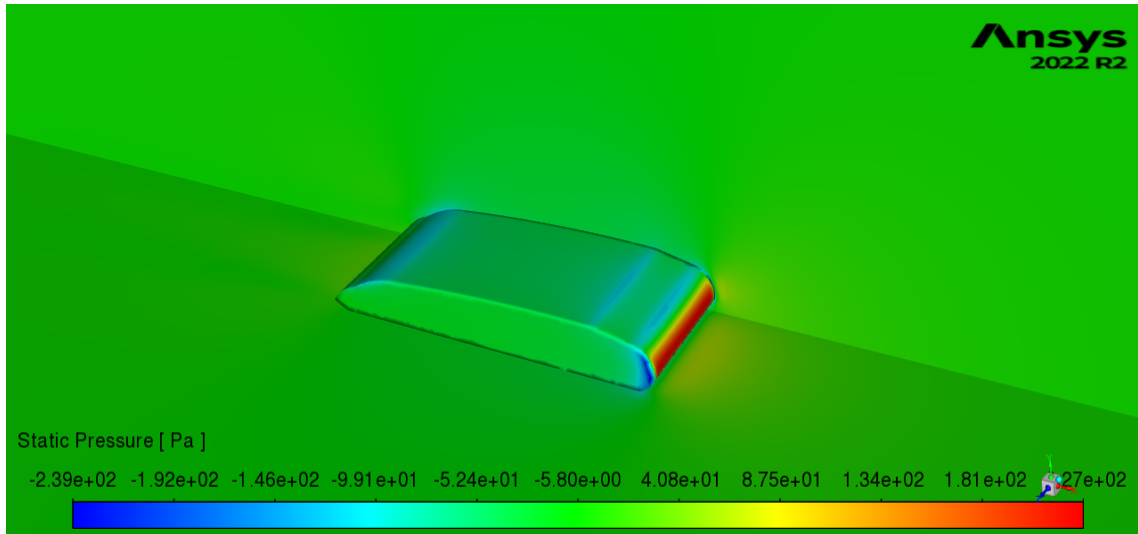


Figure 3.34: Contour of static pressure at failure velocity 0.95 m/s for the hypothetical geobag

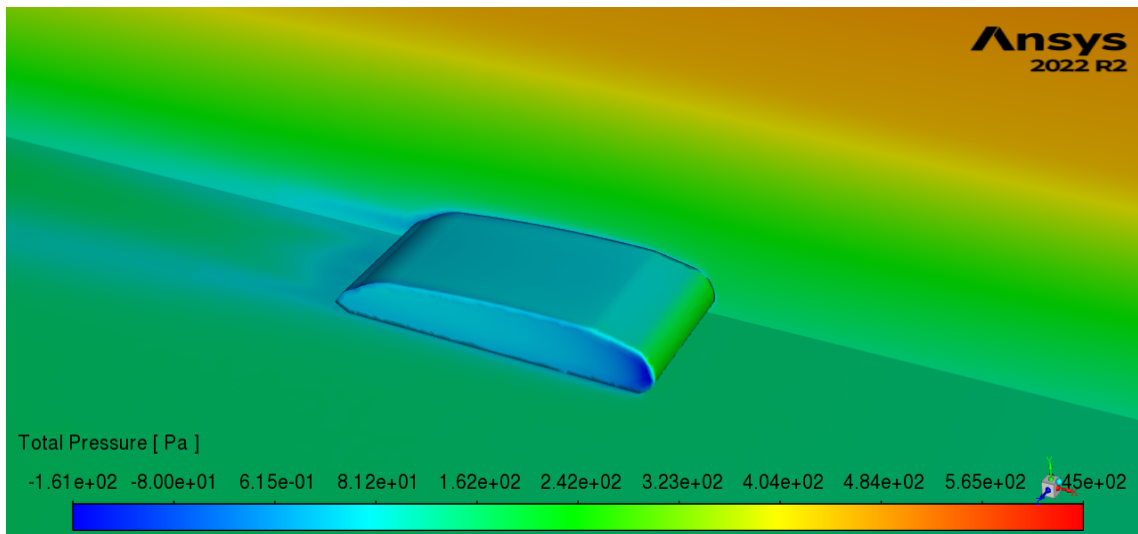


Figure 3.35: Contour of total pressure at failure velocity 0.95 m/s for the hypothetical geobag

Figures 3.36 and 3.37 show the vector plots and pathlines of velocity magnitude at the failure velocity of the hypothetical geobag. According to the plots, no recirculation zone can be observed for the hypothetical geobag, and arrows of the vector plots show areas with lower velocity magnitude around the geobag as a result of no-slip conditions of the geobag.

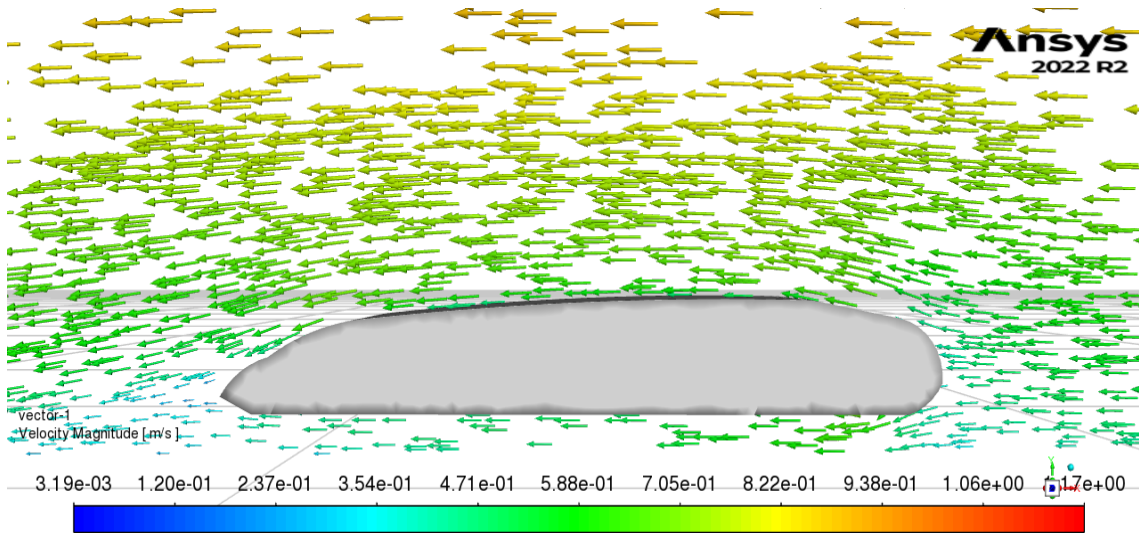


Figure 3.36: Vector plots of velocity magnitude at failure velocity 0.95 m/s for the hypothetical geobag

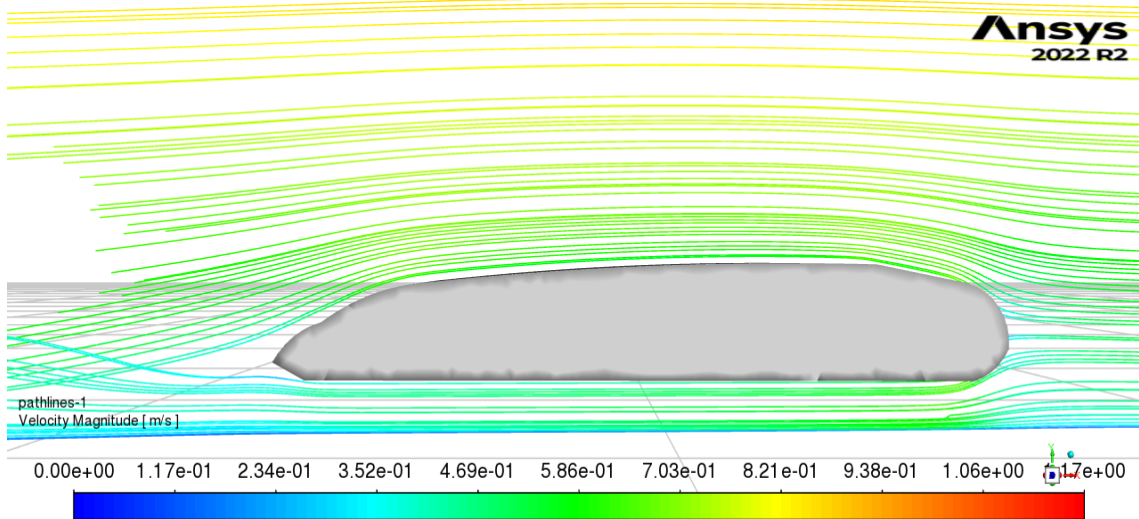


Figure 3.37: Pathlines the velocity profile at failure velocity 0.95 m/s for g1 downstream

Figure 3.38 presents the plot of drag and friction force versus time at the velocity of 0.9 m/s. Since this velocity is less than the failure velocity of the geobag, the friction force becomes more than the drag force, and the bag is not able to move. In contrast, Figure 3.39 shows the plots of drag and friction force versus time at the failure velocity of the geobag, which is 0.95 m/s. The bag only experienced movement at a range of timesteps 0.01 to 0.03 seconds within the timestep of the simulation.

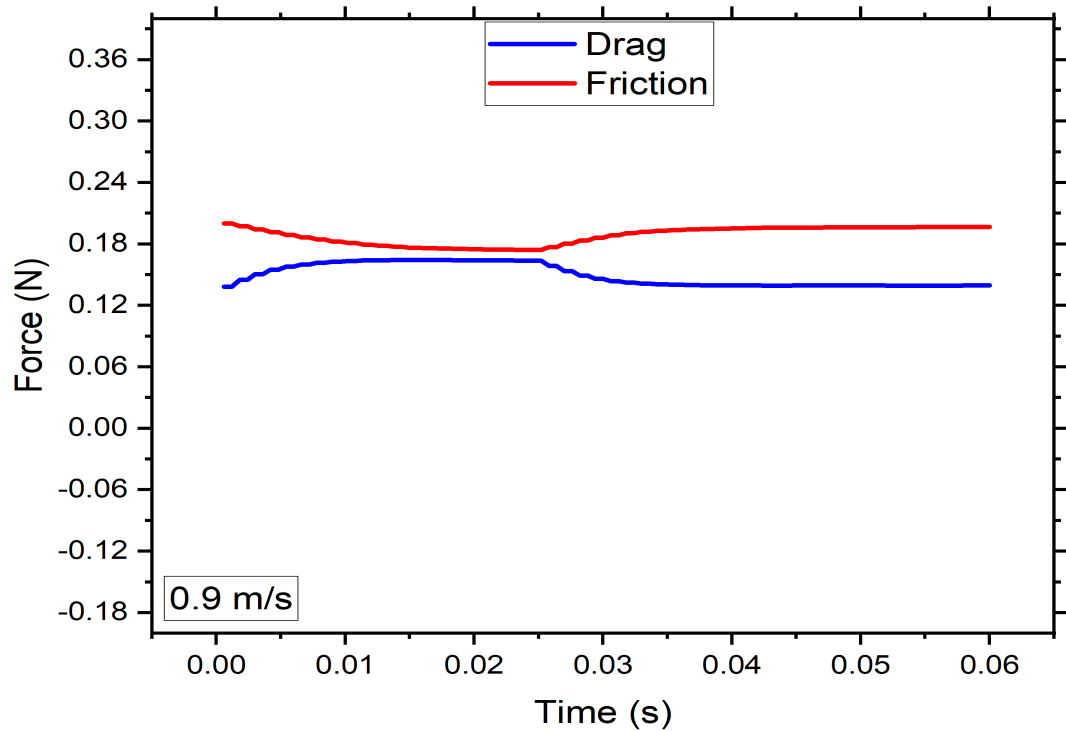


Figure 3.38: Plot of the drag and friction force versus time at a velocity lower than failure 0.9 m/s for the hypothetical geobag

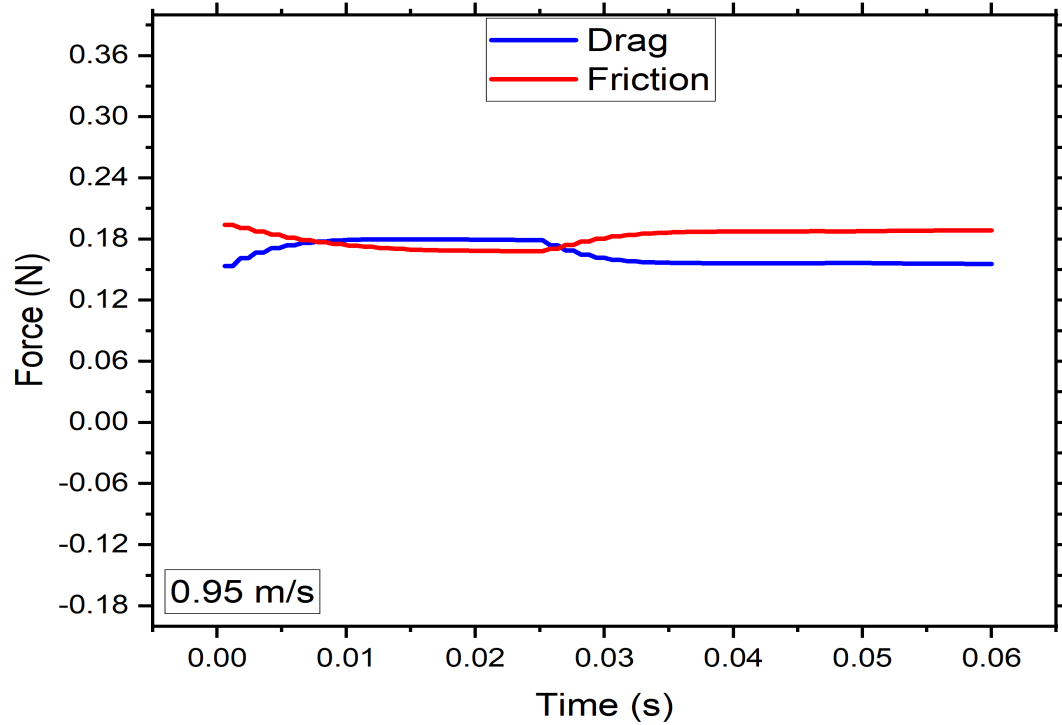


Figure 3.39: Plot of the drag and friction force versus time at failure velocity 0.95 m/s for the hypothetical geobag

In summary, the outcomes of the hypothetical geobag indicate that it is possible to model and determine the failure velocity of geobags that have similar patterns, as presented in Figures 3.2 and 3.3.

# Chapter 4

## Conclusion

### 4.1 Summary

This thesis employs the overset mesh technique to model the behavior of the geobag at the bottom of the channel, aiming to analyze its motion and failure with different materials, shapes, and fill ratios of geobags. The final chapter presented a comprehensive summary of the achievements and conclusions derived from this study.

In the initial phase of this study, the primary objective was to determine the precise shape of the geobags before failure. To accomplish this, an image processing technique was employed to identify the edges of the geobags. Subsequently, the overset mesh technique was utilized to create an accurate model of the geobag positioned at the bottom of the channel. However, it became evident that the overset mesh approach had limitations in effectively modeling the geobag at the bottom of the channel.

To overcome these limitations and achieve a more precise representation, two distinct User Defined Functions (UDFs) were introduced. The first UDF, known as the DEFINE-CONTACT macro, served to establish a threshold distance between the geobag and the bottom of the channel to prevent divergence. The second UDF, known as DEFINE-SDOF-PROPERTIES (6DOF) macro, was responsible for defining the mass and mass moment of inertia of the geobag. Additionally, since the geobag was not ideally situated at the bottom of the channel, the friction force had to be defined as an external force within the 6DOF macro.

Furthermore, the Ansys Fluent used in this study has certain limitations when it comes to accurately incorporating the weight of the bag and calculating the net forces during the simulation. To address this issue, a coefficient referred to as the "effective coefficient" has been introduced. This effective coefficient is carefully defined to ensure the precise determination of the net force in the vertical direction.

In the final phase of this study, the focus shifts to determining the friction coefficient of the geobags, a crucial parameter required for accurately simulating different materials of the geobags at the bottom of the channel.

Once the model was thoroughly verified and validated against experimental data, the subsequent section presents the outcomes of this study:

1. The verification and validation process involves comparing the velocity profiles at various locations of the cement bags with available experimental data. However, it is worth noting that the cloth and geotextile bags were not considered for the verification and validation of the results. The reason for excluding these bags is that they were filled with sand, leading to changes in their shape over time during the experiment. The velocity measurements were taken at the beginning of the experiment when the shape of the bags had not undergone significant alterations. As a result, for the validation of the cloth and geotextile bags with the experimental results, it becomes essential to utilize the initial shape of the geobags at the bottom of the channel. This approach ensures that the validation process accurately reflects the behavior of the bag with the initial shape when the velocity measurements were obtained and minimizes the influence of shape changes during the experiment.

2. This study involved the analysis of 18 geobags used to model the movement of them at the bottom of the channel. Due to filling the bags with sand, their shape undergoes changes during the experiment. However, the simulation did not account for the flexibility of the geobags in the modeling process. Therefore, it becomes crucial

to obtain the precise final shape of the bags before their failure to accurately simulate their behavior. To address this challenge, the image processing technique was employed. This technique enables the accurate determination of the edges and borders of the geobags, thereby providing the exact geometry required for the modeling of the geobags in the channel.

3. To overcome the software limitations in accurately calculating net forces in the vertical direction, an effective coefficient was introduced. This coefficient allows for a precise determination of the friction force, which is calculated by multiplying the net forces in the y-direction with the friction coefficient. A domain is defined for the effective coefficient to ensure that the friction force becomes less than the drag force at failure velocity, allowing for movement of the bag in the flow direction. Conversely, at velocities lower than failure, the effective coefficient was adjusted to make the friction force greater than the drag force, preventing unnecessary bag movements.

4. The experimental part of this study focused on determining the friction coefficients of geobags made from three different materials: cloth, geotextile, and cement bags. The friction coefficient measurements were conducted under two conditions: dry and wet. In dry conditions, the friction coefficient for both geotextile and cloth bags was found to be lower than in wet conditions. This difference can be attributed to capillary pressure within the geobags in unsaturated geobag, leading to increased cohesion and adhesion between the sand grains and the fabric of the geobag. As a result, the friction between the geobag and the inclined surface is higher in wet conditions. On the other hand, for the cement bag, the friction force in wet conditions was observed to be lower than the dry test. This is because water acts as a lubricant between the cement bag and the inclined surface, reducing the frictional resistance.

5. The study revealed that geobags with the same shape before failure exhibited

overlapping ranges of the effective coefficient. This suggests that the failure of the geobags is highly dependent on their final shape before reaching the failure point.

6. This thesis investigated the effects of different materials on the geobag to understand how the material of the bag can affect the motion of geobag at the bottom of the channel. The cloth bags are more stable than their geotextile bag counterpart. This is because the cloth bags either compressed or folded before failure due to the higher flexibility of cloth bags whereas the geotextile bags began to lift from to upcoming flow. Therefore, the lift force plays a key role in the failure of geotextile bags and contributes to lower stability of geotextile bags compared with cloth bags.

7. Three geotextile bags with varying filling ratios were tested to examine the impact of filling ratio and weight on the stability of the geobags. It was observed that geobags with lower fill ratios move at lower velocities. This could be explained by static pressure affecting the geobag. The upcoming flow causes areas with high pressure upstream of the bag and as the fluid flows to the downstream side, the static pressure decreases and creates areas with lower pressure downstream. the pressure difference causes pressure drag. In addition, the area of low pressure on top of the upstream causes sucking up the bag and bags to become lighter, and the friction force decreases as a result of increasing lift force, which makes the bag move even with a lower drag force.

8. This study investigated the impact of the shape of geotextile bags using a single geobag with three different shapes: downstream, even, and upstream shape. The findings indicated that the upstream shape of the geobag required higher failure velocities to initiate movement in the direction of the flow. This can be attributed to the higher density of the bag on the side of the upcoming fluid flow, leading to increased resistance and requiring greater forces for beginning the movement. Conversely, the

downstream shapes exhibited movement at considerably lower failure velocities. This is because of the lift force affecting the geotextile bags. Since the geotextile bag has less flexibility, it experiences lifting due to the incoming flow. The lift force makes that bag move at lower velocities.

10. In the concluding phase of this thesis, a hypothetical geobag was created based on the patterns observed in the geobags investigated throughout the study. Notably, it was observed that it is feasible to determine the failure velocities of any geobag that follows the same shape as presented in this study.

## 4.2 Future works

Finally, some suggestions for further research are presented here:

1. The simulation faced several challenges arising from the limitations of Ansys Fluent in modeling solid bodies at the bottom of the channel using dynamic mesh techniques. For future research, it would be beneficial to explore alternative software options with superior capabilities for modeling solid bodies within the fluid flow, such as STAR-CCM+.

2. In this study, the flexibility and deformation of the geobags were not taken into account during the modeling process. To address this limitation in future research, a promising approach would be to incorporate Fluid-Structure Interactions (FSI) techniques. By utilizing FSI, the modeling can accurately consider the dynamic behaviour, flexibility, and deformation of the geobags in response to fluid flow conditions, providing a more comprehensive and realistic representation of their performance.

3. This study solely focuses on modeling cloth and geotextile bags. However, for future research, it would be beneficial to explore the effects of using different materials for geobags in simulations.

4. The present study focused solely on investigating geobags on a flat channel. However, for future research, a valuable extension could be modeling geobags on inclined surfaces. This would allow us to observe and analyze the effects of the angle of the inclined surface on the failure of geobag.

# Bibliography

- [1] S. J. Restall, L. Jackson, G. Heerten, and W. Hornsey, “Case studies showing the growth and development of geotextile sand containers: An australian perspective,” *Geotextiles and Geomembranes*, vol. 20, no. 5, pp. 321–342, 2002.
- [2] W. Hornsey, J. Carley, I. Coghlan, and R. Cox, “Geotextile sand container shoreline protection systems: Design and application,” *Geotextiles and Geomembranes*, vol. 29, no. 4, pp. 425–439, 2011.
- [3] S. Giri, A. Thompson, G. Donchyts, K. Oberhagemann, E. Mosselman, and J. Alam, “Stabilization of the lower jamuna river in bangladesh—hydraulic and morphological assessment,” *Geosciences*, vol. 11, no. 9, 2021, issn: 2076-3263. DOI: 10.3390/geosciences11090389. [Online]. Available: <https://www.mdpi.com/2076-3263/11/9/389>.
- [4] K. Oberhagemann and M. M. Hossain, “Geotextile bag revetments for large rivers in bangladesh,” *Geotextiles and Geomembranes*, vol. 29, no. 4, pp. 402–414, 2011.
- [5] E. M. MACDONALD, “Flood and riverbank erosion risk management investment program (fermip) project-1,” 2020.
- [6] M. van der Wal, “Bank protection structures along the brahmaputra-jamuna river, a study of flow slides,” *Water*, vol. 12, no. 9, p. 2588, 2020.
- [7] A. Bezuijen, H. d. Adel, M. B. d. Groot, and K. W. Pilarczyk, “Research on geocontainers and its application in practice,” in *Coastal Engineering 2000*, 2001, pp. 2331–2341.
- [8] N. Kobayashi and B. K. Jacobs, “Experimental study on sandbag stability and runup,” in *Coastal Zone ’85*, ASCE, 1985, pp. 1612–1626.
- [9] J. Recio and H. Oumeraci, “Process based stability formulae for coastal structures made of geotextile sand containers,” *Coastal Engineering*, vol. 56, no. 5-6, pp. 632–658, 2009.
- [10] P. Van Steeg and A Bezuijen, “Large scale physical model tests on sand filled geotextile tubes and containers,” in *9th International conference on geosynthetics—geosynthetics: advanced solutions for a challenging world, ICG*, 2010.
- [11] R. Ray, “A laboratory study of the stability of sand-filled nylon bag break-water structures.,” COASTAL ENGINEERING RESEARCH CENTER FORT BELVOIR VA, Tech. Rep., 1977.

- [12] B. K. Jacobs and N. Kobayashi, *Sandbag Stability and Wave Runup on Beach Slopes*. Ocean Engineering Program, Department of Civil Engineering, University of . . . , 1983.
- [13] F. Saathoff, H. Oumeraci, and S. Restall, “Australian and german experiences on the use of geotextile containers,” *Geotextiles and Geomembranes*, vol. 25, no. 4-5, pp. 251–263, 2007.
- [14] A. Bezuijen, M. De Groot, M. K. Breteler, and E. Berendsen, “Placing accuracy and stability of geocontainers,” in *Proc. EuroGeo*, vol. 3, 2004.
- [15] J. Grüne, U. Sparboom, R. Schmidt-Koppenhagen, Z. Wang, and H. Oumeraci, “Stability tests of geotextile sand containers for monopile scour protection,” in *Coastal Engineering 2006: (In 5 Volumes)*, World Scientific, 2007, pp. 5093–5105.
- [16] L. A. Jackson, R. Tomlinson, J. McGrath, and I. Turner, “Monitoring of a multi functional submerged geotextile reef breakwater,” in *Coastal Engineering 2002: Solving Coastal Conundrums*, World Scientific, 2003, pp. 1923–1935.
- [17] D. Dassanayake and H. Oumeraci, “Design and construction aspects of fully submerged geotextile sand container (gsc) structures: Sinking behaviour and deformation of gscs,” Aug. 2010.
- [18] K. G. Shirlal and R. R. Mallidi, “Physical model studies on stability of geotextile sand containers,” *Procedia Engineering*, vol. 116, pp. 567–574, 2015.
- [19] J. Porraz, A. Maza, A. Jose, R. Medina, *et al.*, “Mortar-filled containers, lab and ocean experiences,” in *Coastal Structures’ 79*, ASCE, 1979, pp. 270–289.
- [20] L. Zhu, J. Wang, N.-S. Cheng, Q. Ying, and D. Zhang, “Settling distance and incipient motion of sandbags in open channel flows,” *Journal of waterway, port, coastal, and ocean engineering*, vol. 130, no. 2, pp. 98–103, 2004.
- [21] J. Recio and H. Oumeraci, “Hydraulic stability of geotextile sand containers for coastal structures—effect of deformations and stability formulae,” in *Coastal Engineering 2008: (In 5 Volumes)*, World Scientific, 2009, pp. 3805–3817.
- [22] M. Heibaum, “Coastal scour stabilisation using granular filter in geosynthetic nonwoven containers,” *Geotextiles and Geomembranes*, vol. 17, no. 5-6, pp. 341–352, 1999.
- [23] J. Recio and H. Oumeraci, “Effect of deformations on the hydraulic stability of coastal structures made of geotextile sand containers,” *Geotextiles and geomembranes*, vol. 25, no. 4-5, pp. 278–292, 2007.
- [24] H. Kim, S. Yoo, S. Park, J. Lee, and C. Lee, “A fundamental approach for an investigation of behavior characteristics of the vegetation structures using seeded sandbags,” *Korea*, 2004.
- [25] T. Krahn, J. Blatz, R. Bathurst, and M. Alfaro, “Assessment of sandbag dike interface shear using two direct shear devices,” in *57th Canadian Geotechnical Conference*, 2004.

- [26] K. Pilarczyk, *Geosynthetics and geosystems in hydraulic and coastal engineering*. CRC Press, 2000.
- [27] E Mori, P. Amini, and C. Eliso, “Field experiment on a groin system built with sand bags,” in *International Conference on Coastal Engineering*, 2008, p. 219.
- [28] H Oumeraci, M Hinz, M Bleck, and A Kortenhau, “Sand-filled geotextile containers for shore protection,” *COPEDEC VI, Colombo, Sri Lanka*, 2003.
- [29] N. Nhc, “Jamuna-meghna river erosion mitigation project part b. special report 11, physical model study (vancouver, 458 canada), final report, government of the people’s republic of bangladesh, asian development bank and bangladesh water 459,” *Development Board*, vol. 460, 2006.
- [30] R Mayerle, S. Wang, and F. Toro, “Verification of a three-dimensional numerical model simulation of the flow in the vicinity of spur dikes,” *Journal of Hydraulic Research*, vol. 33, no. 2, pp. 243–256, 1995.
- [31] J. G. Duan, L. He, X. Fu, and Q. Wang, “Mean flow and turbulence around experimental spur dike,” *Advances in Water Resources*, vol. 32, no. 12, pp. 1717–1725, 2009.
- [32] M. Aamir and N. Sharma, “Riverbank protection with porcupine systems: Development of rational design methodology,” *ISH Journal of Hydraulic Engineering*, vol. 21, no. 3, pp. 317–332, 2015.
- [33] Z. Gao, X. Li, H.-w. Tang, and Z.-h. Gu, “Three-dimensional hydrodynamic model of concrete tetrahedral frame revetments,” *Journal of marine science and application*, vol. 8, no. 4, pp. 338–342, 2009.
- [34] R. Kakati, V. Chembolu, and S. Dutta, “Experimental and numerical investigation of hybrid river training works using openfoam,” *Water Resources Management*, vol. 36, no. 8, pp. 2847–2863, 2022.
- [35] A. Thompson, K. Oberhagemann, and Y. She, “Geobag stability for riverbank erosion protection structures: Physical model study,” *Geotextiles and Geomembranes*, vol. 48, no. 1, pp. 110–119, 2020.
- [36] K. White, “Physical study of geobag stability for erosion protection applications in rivers,” 2022.
- [37] A. Thompson, Y. She, and K. Oberhagemann, “Geobag stability for riverbank erosion protection structures: Numerical model study,” *Geotextiles and Geomembranes*, vol. 48, no. 5, pp. 703–712, 2020, ISSN: 0266-1144. DOI: <https://doi.org/10.1016/j.geotextmem.2020.04.004>. [Online]. Available: <https://www.sciencedirect.com/science/article/pii/S0266114420300522>.
- [38] A. Akter, M. Crapper, G. Pender, G. Wright, and W. Wong, “Modelling the failure modes in geobag revetments,” *Water Science and Technology*, vol. 65, no. 3, pp. 418–425, 2012.
- [39] A. Akter, G. Pender, G. Wright, and M. Crapper, “Performance of a geobag revetment. i: Quasi-physical modeling,” *Journal of Hydraulic Engineering*, vol. 139, no. 8, pp. 865–876, 2013.

- [40] S. Verma and A. Hemmati, “Performance of overset mesh in modeling the wake of sharp-edge bodies,” *Computation*, vol. 8, no. 3, p. 66, 2020.
- [41] W.-k. Meng, C.-h. Yu, J. Li, and R.-d. An, “Numerical simulations of air-water flow and rigid-body motion based on two-liquid clsvof/ib method and overset mesh,” English, *Ocean Engineering*, vol. 256, 2022, Air-water flow;Air-water two phase flows;CLSVOF;Dam-break flow;Fluid-structure interaction;Immersed boundary methods;Overset mesh;Rigid body;Two-liquid;Water-water; ISSN: 00298018. [Online]. Available: <http://dx.doi.org/10.1016/j.oceaneng.2022.111455>.
- [42] M. Rashid, B. Ram, R. S. Batth, N. Ahmad, H. M. E. I. Dafallaa, and M. B. Rehman, “Novel image processing technique for feature detection of wheat crops using python opencv,” in *2019 International Conference on Computational Intelligence and Knowledge Economy (ICCIKE)*, IEEE, 2019, pp. 559–563.
- [43] R. Featherstone, *Rigid body dynamics algorithms*. Springer, 2014.
- [44] J. Recio and H. Oumeraci, “Processes affecting the hydraulic stability of coastal revetments made of geotextile sand containers,” *Coastal Engineering*, vol. 56, no. 3, pp. 260–284, 2009.
- [45] L. Khajenoori, G. Wright, and M. Crapper, “Laboratory investigation of geobag revetment performance in rivers,” *Geosciences*, vol. 11, no. 8, p. 304, 2021.
- [46] M. L. Buckley, Y. Wei, B. E. Jaffe, and S. G. Watt, “Inverse modeling of velocities and inferred cause of overwash that emplaced inland fields of boulders at anegada, british virgin islands,” *Natural Hazards*, vol. 63, pp. 133–149, 2012.
- [47] A. Algadi, “Computational fluid dynamics (cfd) based investigations on the flow of capsules in vertical hydraulic pipelines,” Ph.D. dissertation, University of Huddersfield, 2017.
- [48] R. Ulusay and H. Karakul, “Assessment of basic friction angles of various rock types from turkey under dry, wet and submerged conditions and some considerations on tilt testing,” *Bulletin of Engineering Geology and the Environment*, vol. 75, pp. 1683–1699, 2016.